_____
Signature of Supervisor

TU WIEN

**TECHNISCHE
UNIVERSITÄT
WIEN**
Vienna University of Technology

Master's Thesis

DEVELOPMENT OF AN ULTRA-COMPACT SETUP FOR MEASURING ION-INDUCED ELECTRON EMISSION STATISTICS

at the

Vienna University of Technology

Faculty of Physics

Institute of Applied Physics

supervised by

Univ.Prof. Mag.rer.nat. Dipl.-Ing. Dr.techn. Friedrich Aumayr

Dipl.Ing. Dr.techn. Walter Meissl

by

Dominik Schrempf, 0628175

Wichtelgasse 6/22, 1160 Wien

Vienna, February 13, 2013

_____
Signature of Student

Zusammenfassung

Wichtige Untersuchungen von Prozessen bei Elektronenemission, welche durch das Auftreffen von energiegeladenen Teilchen (Ionen, Atomen oder Elektronen) auf Oberflächen hervorgerufen wird, basieren auf der Analyse der Statistik der Elektronenemission (EES). In dieser Masterarbeit wird eine neue und kompakte Version einer EES Anlage präsentiert. Die neue Messelektronik benötigt keine sperrigen "Nuclear Instrument Module" (NIM) mit Netzgeräten, die auf Hochspannung betrieben werden müssen. Stattdessen wurden diese Bauteile durch kleinere und billigere Komponenten ersetzt, die nur mit Batterien betrieben werden können. Das elektronische Signal vom Detektor wird so schnell wie möglich digitalisiert. Sogar die Pulshöhenanalyse wird nun im Hochspannungskäfig durchgeführt und nur das Pulshöhenspektrum wird über optische Kabel zum Messcomputer gesendet.

Die Leistungsfähigkeit der EES Messelektronik wird mit Messungen von ioneninduzierter Elektronenemission von einem Gold-Einkristall getestet. Die neu gemessenen Elektronen-Yields von Ar^{q+} ($q \leq 9$) Ionen, die auf die Goldprobe auftreffen, stimmen mit bereits in der Literatur vorhandenen Daten sehr gut überein. Damit kann bestätigt werden, dass die neue Elektronik funktioniert und richtige Ergebnisse liefert.

Darüber hinaus wurden neue systematische Messungen an Duran®-Glas durchgeführt, um mehr Informationen über die Elektronenemission von diesem Nichtleiter zu erhalten. Duran®-Glas wird benutzt, um makroskopische Glaskapillaren herzustellen, mit denen Ionen umgelenkt werden ("Ion Guiding Effekt"). Verschiedene Messungen wurden am Glas gemacht, um diesen Effekt besser zu verstehen. Dabei wurde der Elektronen-Yield von Ar^{q+} ($q \leq 9$) Ionen, die auf die Glasprobe treffen, in Abhängigkeit von der Temperatur des Glases und in Abhängigkeit vom Auftreffwinkel der Ionen gemessen. Außerdem wurden Messungen in Abhängigkeit von der Geschwindigkeit der Projektile durchgeführt. Es wurde eine starke Temperaturabhängigkeit im Bereich von 20 °C bis 35 °C gefunden. Zusätzlich wurden die Messungen mit bereits vorhandenen Daten von LiF verglichen und die funktionellen Abhängigkeiten bestätigt. Die Resultate und Diskussionen, die in dieser Arbeit präsentiert werden, sollen Fortschritte in der Forschung zum "Guiding Effekt" ermöglichen.

Schlussendlich erleichtert die neu konstruierte Messelektronik die Installation von Anlagen zur Elektronenemission in anderen Labors. Das neue System bietet Mobilität, Flexibilität und bessere Messbedingungen. Die kompakte Gestaltung könnte anderen Arbeitsgruppen die Verwendung der EES Technik für die Analyse von Oberflächenstrukturen und grundlegenden Wechselwirkungen von Ionen mit Oberflächen ermöglichen.

Abstract

Important studies on electron emission phenomena due to energetic projectile impact (ions, atoms, electrons) on both, conducting and insulating surfaces are based on the so-called electron emission statistics (EES) technique. In this thesis a new and compact version of such an electron emission statistics (EES) detection scheme is presented. The new system no longer requires a heavy and bulky NIM-crate with a power supply to be operated at high voltage potential. Instead, these parts have been replaced by small and low cost electronic components, which can be operated using battery packs only. The electronic signal from the passivated implanted planar silicon (PIPS) detector is digitized as early as possible. Even the pulse height analysis is now performed at high voltage and just the resulting pulse height spectrum is communicated by optical fibers to the measurement computer at ground potential.

The performance of the EES detection electronics is tested by ion-induced electron emission studies from a Au single crystal sample. The newly measured total electron yields from Ar^{q+} ($q \leq 9$) ions impinging on the Au sample compare very well with data from the literature. This demonstrates, that the newly built detection setup performs properly.

Furthermore, new systematic measurements were conducted on Duran® glass (borosilicate glass) to get more insight into the electron emission of this insulator. Duran® glass is used for the production of macrocapillaries that guide highly charged ions (HCIs). To get a more profound understanding of the guiding effect, the total electron yield of Ar^{q+} ($q \leq 9$) ions hitting the glass sample has been measured in dependence on the temperature of the sample and the incident angle of the projectiles as well as in dependence on the velocity of the impinging ions. A strong dependence on the temperature from 20 °C to 35 °C has been found. The accumulated data has been compared with total electron yields from LiF and the functional dependencies have been confirmed. The presented data and the discussion of the electron yields might lead to advances in studies on the guiding effect.

Finally, the newly constructed detection electronics presented in this thesis facilitates the installation of an electron emission detection system at other laboratories. It offers mobility, flexibility and improved measurement conditions. The compact design might allow other groups to easily employ the electron emission statistics technique at their beamlines and use it for diagnostic purposes, surface structure analysis and basic ion-surface collision studies.

Acknowledgments

I would like to use this opportunity to give my thanks to various people for their contributions to this master's thesis.

First of all I want to thank Prof. Friedrich Aumayr for his valuable and constructive suggestions during the development of this research work. He introduced me to the beauty of experimental physics and supported me with enthusiastic encouragement and useful critiques. He also provided me with the opportunity to publish in scientific journals and to attend an international conference. Furthermore, his ability to explain physics problems in a short and understandable way astonished me again and again.

I am particularly grateful for the assistance given by Dr. Walter Meissl as supervisor during part of my work on this thesis. His professional guidance and valuable support together with amusing moments helped me a lot with my work in the laboratory.

I also greatly wish to acknowledge the help provided by Katharina Dobes, Robert Ritter, Elisabeth Gruber and Alexander Fuchs-Fuchs as part of the team of Prof. Friedrich Aumayr at the Insitute of Applied Physics. I appreciate their willingness to give their time and support when I had problems with my experiments.

My special thanks are extended to the staff of the Institute of Applied Physics and in particular to the electronics engineer Paul Berlinger who assisted in designing the new detection electronics.

I would like to thank my fellow students at the Vienna University of Technology and especially Alexander Penn. He enlightened my studies with discussions, music jam sessions and refreshing ideas I would never have dreamed of.

I would like to express my very great appreciation to Eva Soltész for encouraging me when I was desperate because of failing experiments. When I addressed her with my scientific problems, I always found a sympathetic ear. She was there when I needed her.

Finally, I want to deeply thank my family and especially my parents. They proofread the thesis and provided me with valuable comments and assistance. They have been supporting me throughout my life and have put all their energy into the education of their three children. I hope that I make them proud and happy with the completion of this master's thesis. Without them, it would not have been possible.

Acronyms

a.u.	atomic unit
AD	Auger de-excitation
ADC	analog-to-digital converter
AFM	atomic force microscope
AI	auto ionization
amu	atomic mass unit
AN	Auger neutralization
arb.	arbitrary units
BEA	binary encounter approximation
CF	Conflat
cKE	collisional kinetic emission
CM	current measurement
COB model	classical over-the-barrier model
DPP	digital pulse processor
EBIS	electron beam ion source
EBIT	electron beam ion trap
ECR	electron cyclotron resonance
ECRIS	electron cyclotron resonance ion source
EES	electron emission statistics
eKE	electronic kinetic emission
FET	field-effect transistor
FWHM	full width at half maximum
HA	hollow atom

HCI	highly charged ion
HOPG	highly oriented pyrolytic graphite
HV	high voltage
IAP	Institute of Applied Physics
IE	ionization energy
KE	kinetic emission
LLD	lower level discriminator
MCA	multichannel analyzer
MCB	multichannel buffer
MCI	multiply charged ion
NIM	nuclear instrument module
PE	potential emission
PIPS	passivated implanted planar silicon
QRN	quasi resonant neutralization
RD	radiative de-excitation
RI	resonant ionization
RN	resonant neutralization
SOPHIE	source for production of highly charged ions using electron-cyclotron resonance
TOF	time of flight
UHV	ultra high vacuum
ULD	upper level discriminator

Symbols

a_0	Bohr radius of the hydrogen atom
A	area
B	magnetic field
Δ	energy band gap in an insulator
ΔE	energy gain in the staircase model
e	electron charge
$(\frac{dE}{dx})_e$	electronic stopping power
E_F	Fermi energy
E_{kin}	kinetic Energy
ϵ	dielectric function
f	screening function
γ	total electron yield
γ_K	total kinetic electron yield
γ_P	total potential electron yield
$\gamma_{P,a}$	potential electron yield above the surface
$\gamma_{P,b}$	potential electron yield below the surface
γ_P^∞	velocity independent potential electron yield
$\gamma_{P,s}$	potential electron yield at the selvedge
λ_γ	relates the mean value of an EES spectrum to γ
λ_s	screening length
ω	angular frequency
ω_s	surface-plasmon frequency
p_b	backscattering probability
q	charge state of an ion
R	reaction rate
R_c	critical distance in the COB model
R_{nl}	critical distance for non-linear effects
r_s	Wigner-Seitz radius
σ	cross section
U	potential U
v	velocity
v_F	Fermi velocity
V_{grid}	voltage applied at the highly transparent grid

V^I	image potential
V_{rep}	voltage applied at the electron repeller
$V_{atom}^{screened}$	screened atom-atom potential
v_{th}	threshold velocity for kinetic emission (KE)
W	work function
ξ	percentage of deposited energy of backscattered electrons
Z^{q+}	ion of the element Z and positive charge state q
Z	element character or atomic number

Contents

Chapter 1

Introduction

The master's thesis at hand was carried out at the Institute of Applied Physics (IAP) at the Vienna University of Technology in the group of Prof. F. Aumayr. It was supervised by Prof. F. Aumayr and partly by W. Meissl who has longstanding experience with ion-induced electron emission. Together with W. Meissl, I designed and constructed the new beamline and planned the new measurement electronics which was assembled by P. Berlinger. The main goals of the master's thesis were:

- the design and construction of a new, light and cost-effective detection electronics to be used with an ion-induced electron statistics detector setup;

- the debugging and testing of the assembled electronics by measuring the electron emission yield of Au (there exists a lot of data for Au to compare with);

- and the systematic performance of some experiments on Duran glass (borosilicate glass) to get more insight into the electron emission of this insulator which is used for the production of macrocapillaries that guide highly charged ions.

1.1   State of the Art

The interaction of heavy particles as atoms, molecules, positive or negative ions on solid surfaces presents a very interesting research topic. It is of high importance to know and describe the different physical processes that lead to specific surface damages or provide the basis for the emission of photons, electrons and neutral or ionized particles.

Specifically, since sources for the production of highly charged ions are available, the impact of these energetic particles on surfaces has been a field of very active research (see e.g. [1–3] and references therein). Especially for future developments in nuclear fusion, which might become an important source of power in the long term, it is necessary to examine the interaction of a plasma with the surrounding wall [4]. The projectile and target material dependent sputter-yield (i.e. the number of sputtered atoms per incident particle) is a highly investigated property [3] because it determines

the lifetime and the usability of different wall materials used in Tokamaks and Stellarators. Electron emission affects the plasma sheath potentials and thus the incident energy of impinging particles, which on the other hand influences the interaction processes and the sputter-yield.

Another important aspect of the interaction of HCIs with surfaces is the possibility to structure a target material on a nanometer scale (nano-structuring) by HCI or swift heavy ions (SHI) impact (see e.g. [1, 3] and references therein). Although in the semiconductor industry photons or electrons are mainly used as projectiles for lithography, ions would offer some advantages. In particular, nano-hillocks (very small hills) or nano holes were found on surfaces exposed to HCI irradiation [5–8]. The sizes of these nanostructures are proportional to the potential energy of the projectiles [1]. Consequently, basic research on ion-surface interaction could encourage further size reductions of semiconductor devices.

Moreover, it was recently discovered that highly charged ion bombardment of insulating capillaries leads to a self-organized charge-up process that allows the ions to be guided and steered through the capillaries [9–15]. This so-called guiding effect depends strongly on different variables like the capillary material, the temperature and the size, type and angle of the capillary. Active research on this effect and its dependencies is currently being conducted (see [14] and references therein).

For the reasons given above research on HCIs and especially on ion-induced electron emission [16–19] is very important. Chapter 2 gives detailed information on highly charged ions and their interaction with surfaces. The theoretical and experimental understanding of the ion induced electron yield, the average number of emitted electrons per ion impact, and its emission statistics is a crucial step towards new industrial applications. The next section 1.2 will provide a short introduction into this very fascinating topic.

On the whole, at our group a considerable amount of work has been invested on electron emission [20–24] and first measurements on the electron yield of LiF [16, 17, 25–27] have been published. Yet, there is still a lot of work to be done. Specifically, we do not fully understand the interactions of highly charged ions with insulators and cannot directly link material constants with the corresponding total electron yields.

1.2 Electron Yield and Emission Statistics

Particle-induced electron emission is of special relevance for the registration of extremely small particle currents, for which the statistics of the electron emission plays a crucial role. The electron emission statistics (EES) (cf. section 2.8), i.e. the probabilities W_n for emission of a given number n of electrons due to a single impact event immediately permits evaluation of the related total electron yield γ as the mean number of

emitted electrons per projectile

$$\gamma \equiv \bar{n} = \sum_{n=0}^{\infty} nW_n = \sum_{n=1}^{\infty} nW_n, \tag{1.1}$$

$$\sum_{n=0}^{\infty} W_n = 1, \tag{1.2}$$

as well as the fraction W_0 of projectiles, which do not emit at least one electron and which are therefore not registered by electron emission.

Important basic investigations on electron emission phenomena during energetic projectile impact (ions, atoms, electrons) have been conducted with an experimental technique, which is able to determine this EES [28–33].

Typical examples for the variety of studies performed with this EES technique are studies on the formation and decay of hollow atoms during highly charged ion impact [2, 34, 35], or investigations on the mechanisms of ion-induced electron emission [16, 25, 27, 36–42]. Some of them employ coincidence measurements between the number of emitted electrons and the angular or energy distribution of the (grazingly) scattered projectiles [43–52]. Since the EES technique is very sensitive (projectile currents of a few particles per second are still sufficient [47]), it is also useful for studies with insulator surfaces [16, 25, 26] where higher primary ion currents would give rise to disturbing surface charge-up phenomena.

Several practical applications of the EES technique have been successfully demonstrated. The strong dependence of the electron emission yield on the charge state and/or impact velocity of the impinging ions was, e.g., utilized to identify and separate ions with identical or very similar mass-to-charge ratio in beams of highly charged ions [53, 54] or clusters [55]. The EES technique, however, cannot only be used as a diagnostic tool for ion beams, but for the bombarded surfaces as well. In so-called ion beam triangulation studies of crystalline surfaces and ultrathin films [56, 57], the change in electron emission during grazing scattering of fast atoms or ions when rotating the target azimuthally (indicating a change from planar to axial channeling [58]), can provide detailed information on the structure of the topmost surface layer [56, 57].

For a more widespread application of such EES techniques it would be of great advantage, if the current rather bulky EES-setup could be replaced by a more compact and less expensive version. In this master's thesis the design of a compact EES detector electronics is described (cf. section 3.6) and its functionality is demonstrated (cf. chapter 4).

1.3 Form and Content

This next section will give the reader a rough overview of the form of this thesis and the content of the different chapters. First, Chapter 2 gives an introduction into the science of ion physics and explains the different processes as well as the theoretical concepts regarding ion-induced electron emission. Then, the experimental setup used

to measure the electron emission statistics and yields will be explained in more detail in chapter 3. Next, chapter 4 thoroughly presents and explains the actual measurements for Duran glass and interprets the obtained results. Finally, conclusions are drawn and possible further work is suggested in chapter 5.

However, to ensure a common theme and to facilitate the reading of this thesis, not all tasks that have been completed during the duration of this thesis are included here. In particular, this concerns the implantation of nitrogen ions into a diamond crystal (documented in [59]).

Finally, a list of abbreviations and symbols used throughout the text can be found at the end of the document. I added their corresponding meaning wherever they are used for the first time. Concerning the documentation of the thesis, I logged everything done in the laboratory in the according logbooks that can be found at "~/data/ES/", where "~" is the home directory of the master's thesis files. Table 1.1 should help to find anything needed for later reference.

Folder name	Content
~/data/	all measured data; it is subdivided into electron emission data (ES) and experimental data regarding the diamond (diamant); it also contains all logbooks that have been written
~/figures/	all figures, graphs and pictures
~/figures-misc/	figures, graphs and pictures not used in the thesis
~/literature/	all papers and books that are cited in the thesis
~/misc/	miscellaneous issues like software (for the DP5 etc.)
~/solidworks/	some CAD files of the sample holder and the electron repeller aperture
~/tex/	the latex files and the pdf of the thesis

Table 1.1: Content of the folders delivered with the thesis.

Parts of this thesis have been submitted for publication and have meanwhile been accepted for publication:

Chapter 2

Highly Charged Ions and their Interaction with Surfaces

This chapter gives a brief introduction into the physics of HCIs and their interaction with surfaces. First, some important aspects of HCIs (cf. section 2.1) including different methods to produce and extract ions will be discussed. Then, after presenting a short overview of ion-surface interactions in section 2.2, I will focus on ion induced electron emission (cf. section 2.3). Finally, I will examine the different contributions of the kinetic and potential electron emission for conductors and insulators.

2.1   Highly Charged Ions

Ions (henceforth denoted as Z^{q+}, where Z is the element and q is the charge state) have already presented an interesting and very complex research topic for more than a century. In contrast to neutral particles, they can be easily manipulated by electric and magnetic fields. Ions with low charge states q are fairly easy to create. Highly charged ions (HCIs), which have been stripped off many electrons (e.g. Xe^{44+}), require more subtle and deliberately designed *ion sources* (cf. section 2.1.1).

In addition to their kinetic energy, ions can also carry intrinsic potential energy, particularly if they have a high charge state. The ionization energy (IE) is the energy needed to remove the outermost electron. It increases rapidly with q. Furthermore, its behavior in dependence on q reflects the atomic shell structure and helps to draw conclusions about the very same. In an HCI, potential energy will be stored according to the sum of the IEs needed to remove q electrons from an originally neutral atom. Figure 2.1 shows the IE and the potential energy in dependence on q. The latter one becomes rather large for high values of q ($E_{pot} > 100$ keV for large charge states) and is available for inducing various inelastic processes upon surface impact, while the HCI will regain its q missing electrons to become fully neutralized again (cf. section 2.2). An ion's charge state cannot exceed its atomic number Z. If $q = $ Z we call the ion a *fully stripped* or *fully ionized* ion. The formation of ion beams takes place in 2 steps:
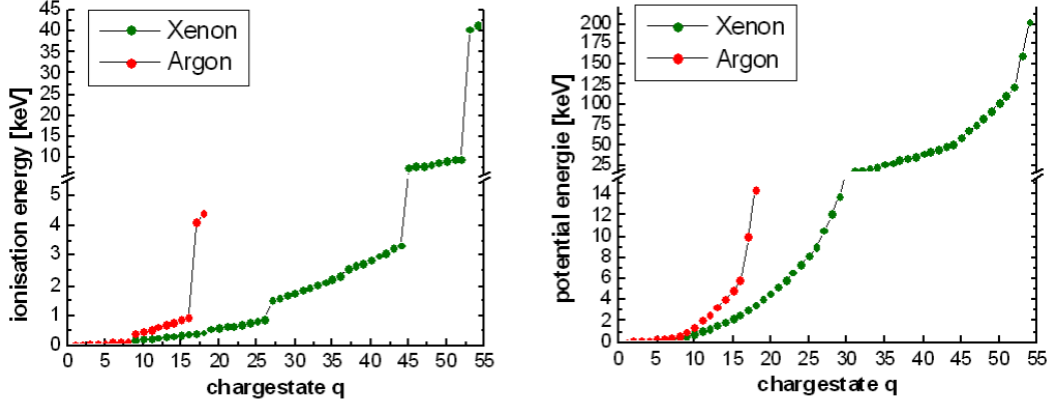
Figure 2.1: IEs (left) and corresponding potential energies (right) for Xenon and Argon ions. Note the jumps of the IE (or the kinks of the potential energies) when an atomic shell has been stripped empty [20, p. 24].

generation of ions in an ion source (cf. section 2.1.1) and the formation of the beam in a beamline (cf. section 2.1.2).

2.1.1 Ion Sources

In the recent years, a high demand for HCIs led to a continuous and strenuous development of ion source technology. HCIs with very high charge states are now available down to low energies. Important characteristics of ion sources include

- the accessible charge states and potential energies

- the minimum and maximum ion current (ions/s) dependent on the charge states and

- the energy distribution of the extracted ions.

One of the most important methods to create ions is electron impact ionization, which follows the following scheme:

$$e^- + Z^{q+} \rightarrow 2e^- + Z^{(q+1)+}. \tag{2.1}$$
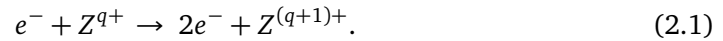
The cross section σ greatly depends on the element species, the charge state of the ion and the energy of the impacting electron, which needs to be higher than the corresponding IE. Usually the cross section reaches a maximum at electron energies 3 to 5 times higher than the IE and then declines with $\frac{\ln E}{E}$. Additionally, for high q values the cross section decreases very fast. The two following ion sources use *step-by-step* ionization to produce HCIs:
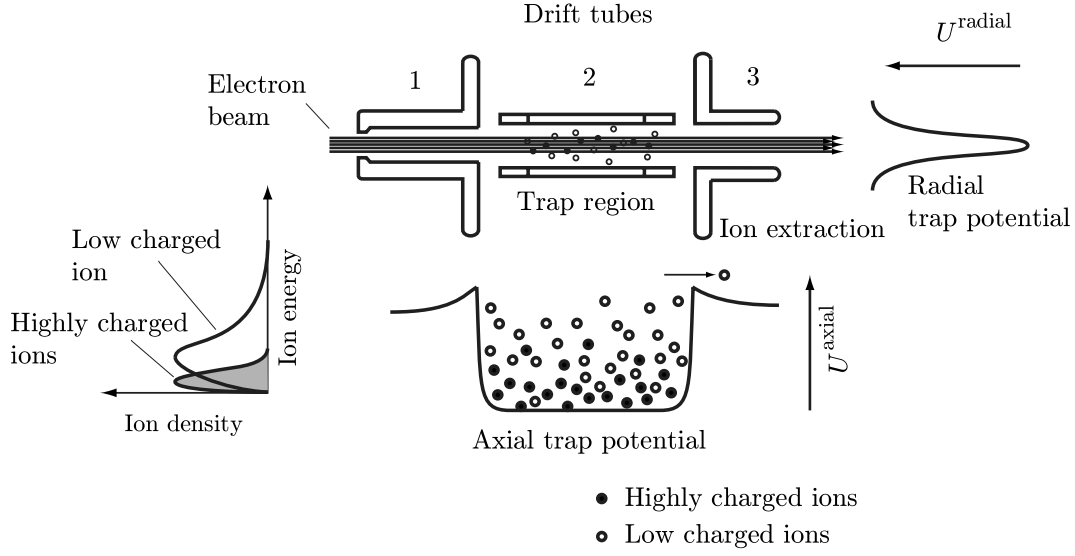
20

Figure 2.2: Principle of an EBIT. The electron beam is accelerated towards the drift tube region. It passes the drift tubes with nearly constant velocity. Around the EBIT the radial potential produced by the space charge of the electron beam and the axial potential generated by the bias voltages applied at the drift tubes are indicated [61].

Electron beam ion trap (EBIT) [60–63]   In an EBIT, the ions to be studied and used are radially trapped by the charge of an ionizing and energetic electron beam and axially trapped by the potential applied to a set of at least three electrodes or drift tubes (cf. fig. 2.2).

For design purposes, the ion-electron reaction rate R can be used as a figure of merit that should be maximized. The reaction rate is defined as

$$R = \sigma_{e-i} n_q n_e v_e A_e, \qquad (2.2)$$

where σ_{e-i} is the cross section of electron impact ionization, $n_{q,e}$ is the number density of ions with charge q or electrons, v_e is the electron velocity, and A_e is the reaction area. Thus, with the electron impact current density $I_e = n_e e v_e A_e$ and $f = \frac{n_q q}{n_e}$, we get [62]

$$R = \frac{\sigma_{e-i} f I_e^2}{q \pi r_0^2 e^2 v_e}, \qquad (2.3)$$

where r_0 is the electron beam radius. This means, that the minimum electron beam radius r_0 with its maximum current density $I_{e_{max}}$ highly influences the maximum reaction rate and therefore the ion source characteristics.

ECRIS [65]   ECRISs are delivering ion beams for a wide range of applications in many laboratories. A charged particle in a static and uniform magnetic field will move in a circle due to the Lorentz force. The angular frequency of this cyclotron motion for a
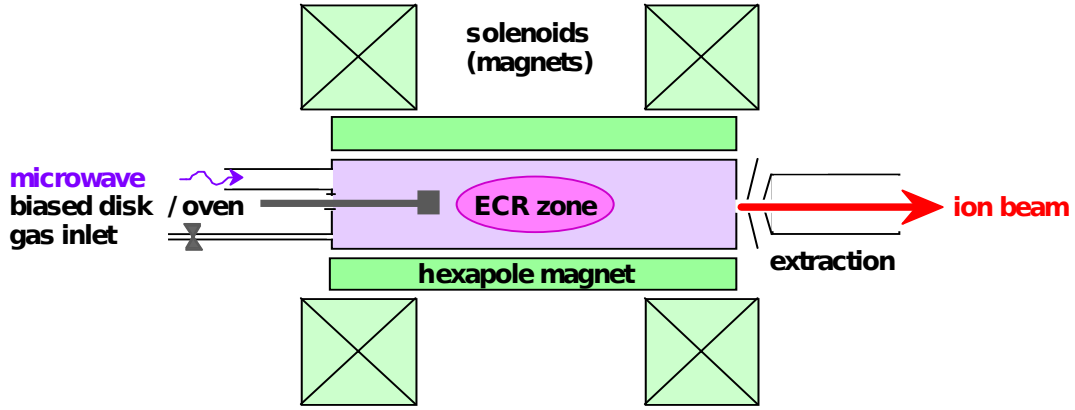
Figure 2.3: Operating principle of an ECRIS [64, p. 5]. Four solenoids and a permanent hexapole magnet create the confining magnetic field. Electromagnetic waves are injected by a traveling wave tube amplifier. The plasma is positively biased and the gas to be ionized is inserted via a gas inlet valve. At the right side an extraction system extracts the ions and forms an ion beam.

given magnetic field strength B and mass m of the particle is given by

$$\omega_c = \frac{qB}{m}.\qquad(2.4)$$

An ECRIS uses this electron cyclotron motion by injecting energy into a confined plasma using microwaves (electromagnetic waves) of suitable frequencies (e.g. 14.5 GHz). This is called *heating* a plasma. If ω_c of the electrons corresponds to the frequency of the injected microwaves, energy is added very effectively, and electron temperatures of some keV (which exceeds the ionization energy) are reached. The electrons themselves ionize the confined ions *step-by-step*. Figure 2.3 shows a schematic overview of an ECRIS. The confining magnetic field is created by solenoids and a permanent hexapole magnet. An electrode system is used to extract the ions (cf. section 2.1.2). For the work on this master's thesis the ECRIS SOPHIE situated in the Augustin laboratory of the Institute of Applied Physics at the Vienna University of Technology (cf. section 3.1) was used.

2.1.2 Ion Beam Formation

After the generation of the ions, they have to be extracted from the source by means of electrostatic fields. Nevertheless, applying certain electrodes for extraction changes the potentials in the source, eventually leading to a withdrawal of the plasma edge. This might lead to a lower ion current or a defocus of the beam. Additionally, due to the ions being a lot heavier than the electrons, the former are slower than the latter ones. The simplest type of extraction system is a diode system consisting of a plasma electrode at positive ion source potential and an extraction or ground electrode at ground potential. An ideal plasma is an equi-potential region. When the plasma stays in contact with an electrode held at a different potential, a sheath is formed, and the whole potential dif-

ference between the plasma and the electrode is localized within this sheath. Electrons
emitted from the plasma are reflected at this boundary if their energy is less than the
potential drop between these two electrodes [64, p. 27].

The extracted ion beam is formed by electrostatic potentials and separated accord-
ing to its charge to mass ratio by an analyzing dipole magnet. Before entering the target
chamber the ions may be accelerated or decelerated to their final energy. An important
characteristic of a strong beam of charged particles is its perveance. It describes the
widening of the beam due to the repelling Coulomb force of the particles.

For nanostructuring and recent studies very slow HCIs are needed. Different *de-
celeration systems* have been designed. In the "Forschungszentrum Rossendorf" near
Dresden, very sophisticated deceleration systems consisting of two or more lenses have
been built [61].

2.2 Ion-Surface Interaction

The irradiation of solids by energetic ions (or atoms) gives rise to a variety of phe-
nomena. The incident particles may be backscattered, electrons or photons emitted,
and target atoms or molecules ejected. The latter process is called sputtering [3]. The
decelerating projectiles transfer energy and momentum to the target atoms in a near-
surface region of the solid, which extends to a depth that depends primarily on the
incident particle's energy and mass. This process may cause rather extensive displace-
ment cascades and point defects [66, p. 7]. The technological relevance of low-energy
ion-surface interactions in such diverse fields as surface analysis, ion-implantation, sput-
ter cleaning of surfaces and thin film deposition has provided the stimulus for ongoing
investigations into the responsible basic mechanisms.

Due to the large number of coupled degrees of freedom, theoretical descriptions of
the scattering of heavy particles at surfaces have remained a challenge. The quantum
mechanical description of an interacting many-body system far from the ground state
excludes the application of ground state theories such as density-functional theory and
models that couple the electronic system near the ground state to a heavy particle
motion. Most models and approximations can be divided into slow and fast collisions.
A collision is denominated slow if the projectile velocity v_p is very small compared
to the characteristic electron velocity. The Fermi velocity v_F is the velocity associated
with the Fermi level of a given material by solving $E_F = \frac{1}{2}m_e v_F^2$. It often represents
the characteristic electron velocity and can be translated to particle energies of about
25 keV/amu (for H the ionization energy corresponding to the Fermi level is 13.6 eV
which translates to a Fermi velocity of about 2.19×10^6 m/s $\equiv$ 1.0 a.u. or 25 keV/amu).
Hence, ions with energies reasonably smaller than 25 keV/amu collide "slowly" with the
target surface.

Nevertheless, due to the anisotropic nature of ion-surface collisions one has to divide
the velocity into a component parallel to the surface $v_{p,\parallel}$ and a component perpendic-
ular to the surface $v_{p,\perp}$ [67, p. 2]. Different measurable quantities separately depend

on $v_{p,\parallel}$ and $v_{p,\perp}$. Closely related to this is the distinction between the kinetic and the potential energy of the impinging particle (cf. sections 2.1, 2.4 and 2.5).

2.3 Ion-Induced Electron Emission

The thesis at hand solely treats electron emission. The theoretical and experimental understanding of the ion induced electron yield, the average number of emitted electrons per ion impact (cf. section 2.8), is a crucial step towards new industrial applications. Electron emission itself can be divided into numerous processes. The next sections will try to give an introduction into the principles and models regarding the interesting measurement observable electron emission yield.

The most important classification of the total ion induced electron emission yield (usually γ) is the distinction between electrons that are emitted due to the kinetic energy and electrons that are emitted due to the potential energy of the impinging particle. The former is called KE (cf. 2.4), the latter potential emission (PE) (cf. 2.5). Hence, we can write

$$\gamma = \gamma_K + \gamma_P. \tag{2.5}$$

All present experimental methods can only determine the total electron yield γ. To be able to distinguish the different emission processes, one has to perform experiments, where either KE or PE dominates. Roughly, PE can be associated with slow collisions of HCIs and KE with fast collisions, where v_p is in the range of v_F or considerably higher. Alternatively, for collisions of ions in lower charge states or even atoms (leading to a complex experimental setup), KE also is the main source of emitted electrons. Clearly, this approximate distinction cannot account for the subtleties of interaction processes and requires revisions and amendments.

2.3.1 Theoretical Concepts and Methods

There exist various theoretical methods which try to solve the difficult problem of ion induced electron emission. Basically, they can be characterized by the degree to which electronic processes are treated classically. In fact, it turned out, that classical approximations are reasonably successful in the description of the electronic dynamics of surface collisions. This section will introduce some important classical concepts and ideas. Atomic units (a.u.) will be used throughout this subsection unless indicated otherwise. For further information consult the very good introduction of Burgdörfer and Lemell that includes a quantum mechanical treatment [67].

One important aspect to understand the interactions of particles near a surface is the determination of the interaction potentials, which serve as input parameter for the calculation of collision processes. A basic approximation uses **image potentials** created by particles near surfaces. For a slow particle with charge q and a large distance z from

a conducting surface, one gets the image potential

$$V^I(z) = -\frac{q^2}{4z}. \tag{2.6}$$

It became apparent, that shifting the effective image plane by z_{im} with respect to the actual jellium edge [68]

$$V^I(z) = -\frac{q^2}{4(z - z_{im})}, \tag{2.7}$$

gives more accurate results. For insulators, eq. (2.7) has to be modified again to [69]

$$V^I(z) = -\frac{q^2}{4z}\frac{\epsilon(\omega) - 1}{\epsilon(\omega) + 1}, \tag{2.8}$$

where ϵ is the dielectric function and ω is the angular frequency of the impinging radiation. Although $\epsilon(\omega)$ is known for most materials, it is still uncertain, which ω has to be chosen, since only one ion hits the surface at a time ($\epsilon(\omega)$ for LiF at 300K varies from 0 to 9, [70]). The classical representations described by eqs. (2.6) to (2.8) are only valid at large distances compared to the characteristic screening length for surface plasmons [69],

$$\lambda_s = \frac{v_F}{\omega_s}, \tag{2.9}$$

where ω_s is the surface-plasmon frequency and v_F is the Fermi velocity of the conduction band (cf. section 2.2). Numerical values for gold are $\omega_{s,Au} \approx 0.3$ a.u. (1.4×10^{16} s^{-1} [71–73]), $v_{F,Au} \approx 0.6$ a.u. (1.4×10^6 m/s [74]) and, hence, $\lambda_{s,Au} \approx 1.9$ a.u. (1.9 a_0, where a_0 is the Bohr radius). Image potentials provide a very effective tool to characterize the dynamics of the electron emission of approaching ions (cf. to the classical over-the-barrier and the staircase models below). For small distances and larger velocities, the **dielectric response** of the target electron gas, which is described by the dielectric function ϵ, has to be taken into account. Both descriptions, the image potential and the dielectric response method are only applicable if the response is linear. Non-linear effects become important at a distance smaller than [75]

$$R_{nl} \approx 2r_s \sqrt{q}, \tag{2.10}$$

where r_s is the Wigner-Seitz radius which is usually between $2.0\,a_0$ and $6.0\,a_0$ [74, ch. 4].

To calculate the trajectory of an ion approaching a surface, the knowledge of the effective ion interaction potential is indispensable. Using a **screened atom-atom potential** is a possibility to approximate the complex ionic potential [76]:

$$V_{atom}^{screened}(r) = \frac{Z_p Z_s}{r} f(r/a_s), \tag{2.11}$$

where $Z_{p,s}$ are the bare nuclear charges of the projectile and surface atoms and f is the screening function.

All the previous methods model the effects of the potential energy stored in an approaching ion. The **binary encounter approximation (BEA)** [77, 78] describes a possible kinetic emission process. In this model, electron excitation results from the screened Coulomb interaction between the projectile (ion) and the target (electron) through direct "binary collisions" and the decay of collective excitations (plasmons). At velocities smaller than v_F, the velocity of the electrons at the Fermi surface, plasmons will be excited inefficiently. The threshold velocity v_{th} for ejection of an electron into vacuum can be calculated by assuming a head-on, elastic collision conserving energy and momentum. Then, the maximum energy transfer equals the work function (W), that is,

$$\Delta E = 2mv_{th}(v_{th} + v_F) = W. \tag{2.12}$$

and, hence [79],

$$v_{th} = \frac{v_F}{2} \left(\sqrt{1 + W/E_F} - 1 \right). \tag{2.13}$$

	LiF(001)	Au	Au(111)	Al
work function W [eV]	12	4.8	5.31	4.3
Fermi energy E_F [eV]	-	5.5	5.5	11.7
Fermi velocity v_F [a.u.]	-	0.64	0.64	0.93
threshold velocity v_{th} [a.u.]	-	0.18	0.2	0.08

Table 2.1: Work function, Fermi energy, Fermi velocity and threshold velocities for different materials [20, 80–82].

Numerical values for e.g. gold and aluminum are (cf. table 2.1): $v_{th,Au} = 0.2$ a.u. and $v_{th,Al} = 0.08$ a.u. (assuming $E_{F,Au} = 5.5$ eV, $W_{Au} = 5.31$ eV, $E_{F,Al} = 11.7$ eV and $W \approx 4.3$ eV [20, 80, 81]; it should be added that measured values for gold differ slightly from the theoretical estimates, e.g. $v_{th,Au}^{exp} = 0.1$ a.u. [83]).

Nevertheless, careful measurements in the threshold region have shown that KE can be observed also for particle velocities $v_p < v_{th}$ [84] because of "umklapp processes", where the absolute threshold is determined from energy conservation alone, resulting in

$$v_{th}^{abs} = \sqrt{2W/M} \tag{2.14}$$

or

$$E_{th}^{abs} = \frac{1}{2}M(v_{th}^{abs})^2 = W, \tag{2.15}$$

where M is the mass of the bombarding ion.

Regarding the PE of electrons from slow HCIs, the **classical over-the-barrier model
(COB model)** was found to be remarkably versatile and successful [85–87]. This model
only considers classically allowed over-the-barrier processes to be sufficiently fast to be
effective within the characteristic interaction time of the ion with the surface. Conse-
quently, quantum tunneling effects are not taken into account. For simplicity, the COB
model chooses Coulomb potentials for all electronic interactions using the image po-
tential method described above. The "active" electron is the electron at distance z from
the surface region, which is to be transferred to the projectile for PE. If an HCI at the
distance R from the jellium edge of a conductor arrives and z,R are large in comparison
to λ_s, the active electron is exposed to a potential [86]

$$V(z) = V_e^I(z) + V_{pe}(z,R) + V_{pe}^I(z,R). \tag{2.16}$$

Here, V_e^I is the image potential of the electron given by

$$V_e^I(z) = -\frac{1}{4z}, \tag{2.17}$$

$V_{pe}(z,R)$ is the potential of the impinging ion with charge q

$$V_{pe}(z,R) = -\frac{q_{eff}}{|z - R|} \tag{2.18}$$

and $V_{pe}^I(z,R)$ is the image potential of the ion

$$V_{pe}^I(z,R) = \frac{\tilde{q}_{eff}}{|z + R|}. \tag{2.19}$$

The values inserted for q_{eff} and $\tilde{q}_{eff}$ can be found in [86]. It should be pointed out, that
there is a difference of the factor $1/4$ between V_e^I and V_{pe}^I. On the one hand, the position
of the image charge of the electron changes with z, but on the other hand, the position
of the image charge of the ion does not. Using eq. (2.16), we can find approximate
analytic expressions for the z coordinate of the saddle point z_S ($\frac{\partial V(z)}{\partial z}\big|_{z_S} \equiv 0$). For
$q \gg 1$ we have

$$z_S \simeq \frac{R}{\sqrt{8q}} \tag{2.20}$$

and the value of the potential at the saddle point

$$V(z_S) \simeq -\frac{1}{2R}\sqrt{8q}. \tag{2.21}$$

The critical distance R_c, where the electron capture process starts is accordingly given
by [86]

$$R_c \simeq \frac{\sqrt{2q}}{W}. \tag{2.22}$$

27

As the projectile ion continues to approach the surface, electrons are transferred resonantly from the surface to the ion. For an accurate description of the dynamics of these processes, the COB model uses rate equations considering the frequencies of resonant neutralization (RN), resonant ionization (RI) and gain and loss due to auto ionization (AI) processes (cf. section 2.5). Additionally, in the staircase approximation of the COB model (the behavior of the effective charge q_{eff} of the ion looks like a staircase), the energy gain of an impinging ion based on its image charge acceleration can be calculated to [88]

$$\Delta E = \frac{W}{3\sqrt{2}} q^{3/2}.$$ (2.23)

It has to be taken into account, that R_c, $V_{pe}(z, R, q)$ and $V_{pe}^I(z, R, q)$ change with subsequent neutralization processes.

For insulators, which have a narrow valence band, a large work function W, and a wide band gap Δ, the critical distance R_c and the total energy gain ΔE corresponding to the staircase model are harder to derive analytically [87, 89, 90]. Hägg et al. [87] present a theoretical analysis of the above-surface processes of HCIs approaching LiF. In summary, they apply eq. (2.16) on an ionic crystal lattice leading to more general interaction potentials. The electronic surface potential ($V_e(z)$, cf. eq. (2.17)) now contains four contributions that describe the interaction between the electron and [87]

(a) the halide at the origin of the coordinate system,
(b) the ionic lattice of the crystal (Madelung potential),
(c) the screened localized positive charge left in the surface and
(d) the image charge of the electron.

On the other hand, the projectile image potential ($V_{pe}^I(z, R)$, cf. eq. (2.19)) includes the dynamic response of the crystal through the inclusion of a frequency-dependent dielectric function $\epsilon(\omega)$. For a constant $\epsilon(\omega) = \epsilon$ (statical limit) the image charge potential [91] can be reduced to eq. (2.8).

Bárány and Setterlind used the classical barrier approach to derive the critical distance for insulating surfaces in the statical limit ($\epsilon(\omega) = \epsilon$):

$$R_c = \frac{\sqrt{2q\epsilon(7 + \epsilon)}}{(\epsilon + 1)W}.$$ (2.24)

Due to the large work function W, the first electron capture occurs much closer to the surface of an insulating sample than to the surface of a conducting one.

This concludes the introduction of theoretical concepts and methods in the classical regime for electron emission on the basis of ion impact. A more profound analysis and some quantum mechanical methods can be found in [67].

2.4 Ion-Induced Kinetic Electron Emission

KE covers events which emit electrons due to the kinetic energy of the impinging particle. Its contribution to the total electron yield γ is high if the particle is an atom or a lowly charged ion and mainly depends on the electronic stopping power S_e [92], e.g. the average energy loss of the impinging ion per unit path length. S_e itself depends on the kinetic energy of the particle and rises more or less linearly for moderate particle energies below approximately 1 MeV per nucleon (depending on the projectile and the target material [93]) where it saturates. For higher kinetic energies S_e drops to lower values and the contribution of KE becomes small again. The emission process results from a large number of scattering and energy-loss processes and generally starts with primary excitation cascades of recoiling target atoms and electrons [66]. Affected electrons may then be transported to the bulk surface eventually exciting secondary electrons during this process. Finally, any of these electrons may cross the solid-vacuum boundary and contribute to the kinetic electron yield γ_K.

As a consequence at least two different mechanisms cause KE [42]. One due to primary ions with velocities greater than a certain minimal threshold impact velocity v_{th} colliding with target electrons (eKE, cf. binary encounter collision model in section 2.3.1). And one principally different process, where electrons are promoted into vacuum by recoiling target atoms and electrons (implicit or collisional kinetic emission (cKE)). Whereas the electronic stopping power $(\frac{dE}{dx})_e$ [92, 94] determines the magnitude of the first part, the nuclear stopping power is related to the second effect which
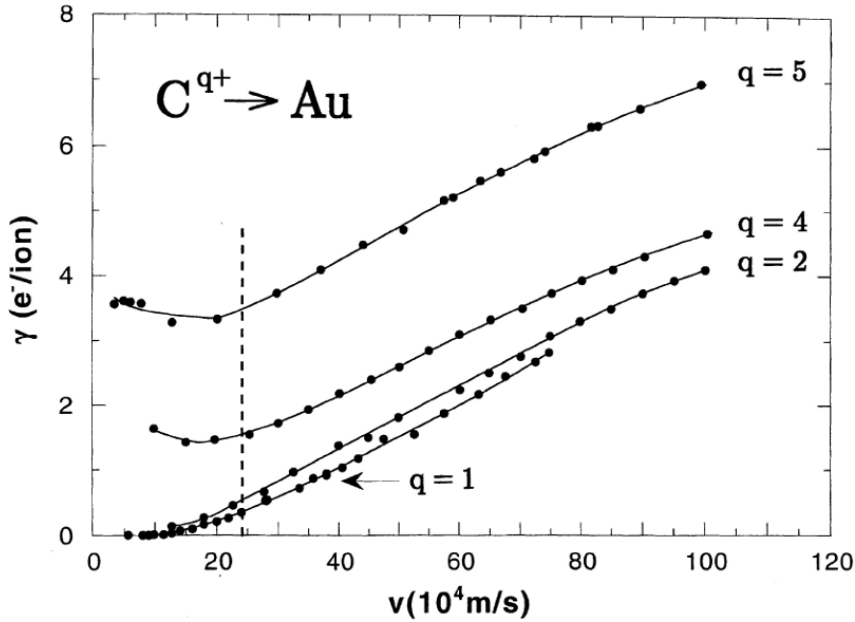

Figure 2.4: Total electron yields γ measured vs. impact velocity v for impact of C^{q+} ($q = 1, 2, 4, 5$) on well conducting, clean and polycrystalline gold (eKE threshold marked by dashed line) [42].
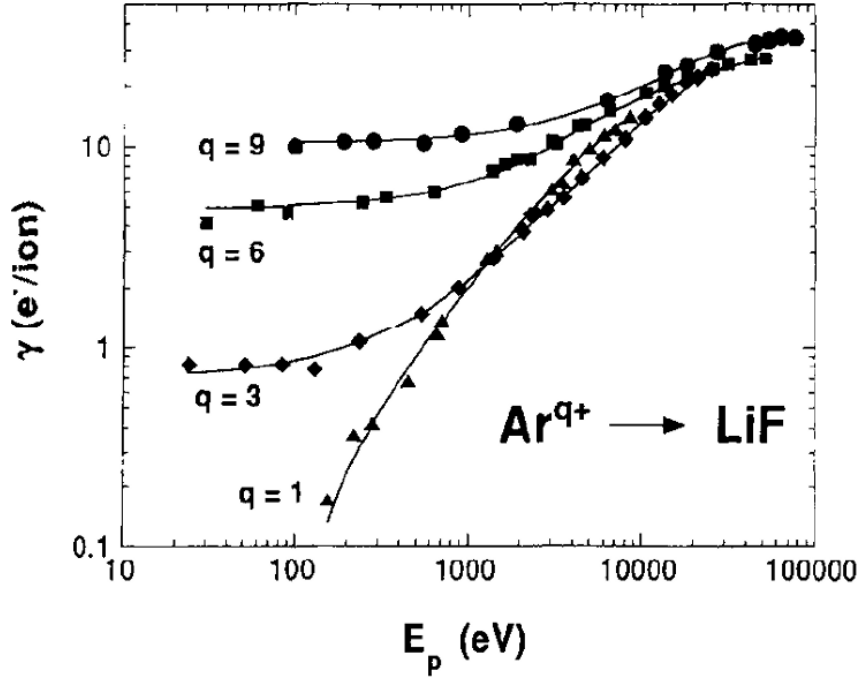
Figure 2.5: Total electron yield γ for impact of Ar^{q+} ($q = 1, 3, 6, 9$) on the wide band gap insulator LiF vs. impact energy E_{kin} [25]. Note that $E_{kin} \propto v^2$.

starts already well below v_{th} for heavy particles. For conducting target materials and ion charge states $q = 1$ to 3 a slight decrease of KE with q has been found, but no significant q dependence could be measured for higher charge states [42]. Bodewits et al. [95] compare the electron yield from new measurements on highly oriented pyrolytic graphite (HOPG) with respect to Au as a function of the kinetic energy.

Interestingly, fairly different kinetic electron yields γ_K were observed for impact on conductor and insulator surfaces. Experiments show, that the tightly bound valence electrons of insulators (binding energies of typically about 10 eV) can be extracted more efficiently than conduction electrons of metals ($W \approx 5$ eV) resulting in higher yields [16,96]. One reason might be that in insulators, the mean free paths of electrons are significantly larger due to the wide band gap .

Velocity Dependence of the Kinetic Electron Yield: The **velocity dependence** of γ_K is of crucial importance and has been investigated by various research groups. Eder et al. [32,42] and Svensson et al. [97] measured electron yields from polycrystalline gold and aluminum respectively and observed a more or less linear increase at moderate impact velocities ($v_{th} < v_{impact} \lesssim 2$ amu). For higher velocities experiments usually show a saturation of the yield (cf. fig. 2.4) and a decline at even higher energies. Data concerning the kinetic yields γ_K of insulators is harder to find. The main reason is that the direct determination of emission yields from insulators using a current method (cf. section 2.7) has only been made available in recent years [17]. Vana et al. [25]

bombarded lithium fluoride with HCIs and found a similar velocity dependence (cf.
fig. 2.5). It has to be pointed out that in experiments with HCIs, it is often hard to
separate γ_P, the yield due to PE, from γ_K [18, 21]. Especially because γ_P uses to be
large for multiply excited atoms and also depends on the velocity (cf. section 2.5).
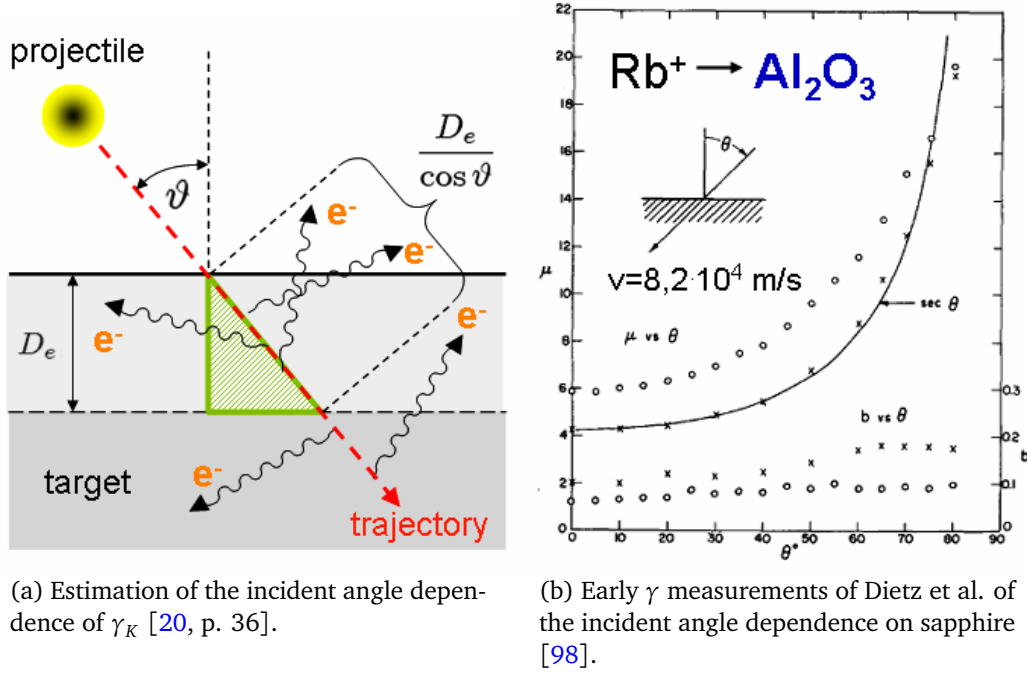

(a) Estimation of the incident angle dependence of γ_K [20, p. 36].

(b) Early γ measurements of Dietz et al. of the incident angle dependence on sapphire [98].

Figure 2.6

Incident-Angle Dependence of the Kinetic Electron Yield: Another very important
aspect is the **dependence of γ_K** on the **incident angle** of the particle. This behavior can
be made plausible using simplified assumptions (cf. fig. 2.6). Firstly, recoiling electrons
have a certain elastic mean free path $\lambda_e(E_e)$ dependent on the energy of the electron
and the material. Secondly, the projectile hitting the target enters deeper than this
elastic mean free path and thirdly, it excites electrons continuously on its path. Then,
the amount of emitted electrons is roughly proportional to the length of the trajectory
in the surface layer of thickness D_e. This leads directly to

$$\gamma_K(\theta) \propto \frac{c_K}{\cos\theta}, \tag{2.25}$$

where θ is the incident angle and c_K is the electron yield for perpendicular incidence
($\theta = 0°$). In general, c_K is considerably higher for insulators because $\lambda_e(E_e)$ is larger
[21, p. 76]. Indeed, the first angle dependence measurements have been made using
electron emission statistics (cf. Dietz et al. [98], fig. 2.6). Apart from the elastic mean

31

free path $\lambda_e(E_e)$, experiments suggest that a second determining parameter of KE is the work function W_Φ of the target material. An overview of the velocity and angle dependence of metals and insulators for PE and KE is given in section 2.6.

KE below the threshold velocity and its behavior at this velocity regime constitutes a very promising research topic. Total electron yields for these measurements are usually very low and require the use of neutral particles as projectiles and the utilization of a very accurate measurement system. A general introduction on KE with emphasis on these difficulties gives [99]. Theoretic calculations confirm the emission of electrons below the threshold velocity (cf. [100]).

2.5 Ion-Induced Potential Electron Emission

Potential emission (PE) covers events which emit electrons due to the potential energy of the impinging particle. This stored energy can be very high (cf. section 2.1) and might exceed the kinetic energy by far for projectiles in high charge states. Due to potential yields γ_P increasing strongly with the carried potential energy, γ_P might be much larger than γ_K. A short but instructive introduction into PE gives [2]. In contrast to KE, which solely occurs inside the solid, PE can be divided into three stages:

- emission of electrons before impact $\gamma_{P,a}$ ("a" for "above surface"),

- "peeling off" of highly excited Rydberg electrons at the target selvedge $\gamma_{P,s}$ and

- electron capture into inner vacancies accompanied by slow secondary electron emission already below the surface $\gamma_{P,b}$.

Summing up, γ_P can be written as [42]

$$\gamma_P = \gamma_{P,a} + \gamma_{P,s} + \gamma_{P,b}. \tag{2.26}$$

Figure 2.7 gives an overview of the different processes which take part during the impact of a HCI on a surface. Hagstrum [101–103] was among the first to analyze potential electron emission of conductors. The various possible transitions, that he introduced, are explained in more detail below. Although most of the following considerations have been done for conductors, they are similarly applicable to insulator targets.

All in all, electronic transitions of an excited atom or ion can be of the resonance, Auger and radiative types. Due to the lifetime of electronic states in high n shells (10^{-8} s), radiative transitions can be ruled out as a significant competing process to electron emission. This means, that only four basic processes remain: resonant neutralization (RN) and resonant ionization (RI) as well as Auger neutralization (AN) and Auger de-excitation (AD). For details see [2, 101–103].
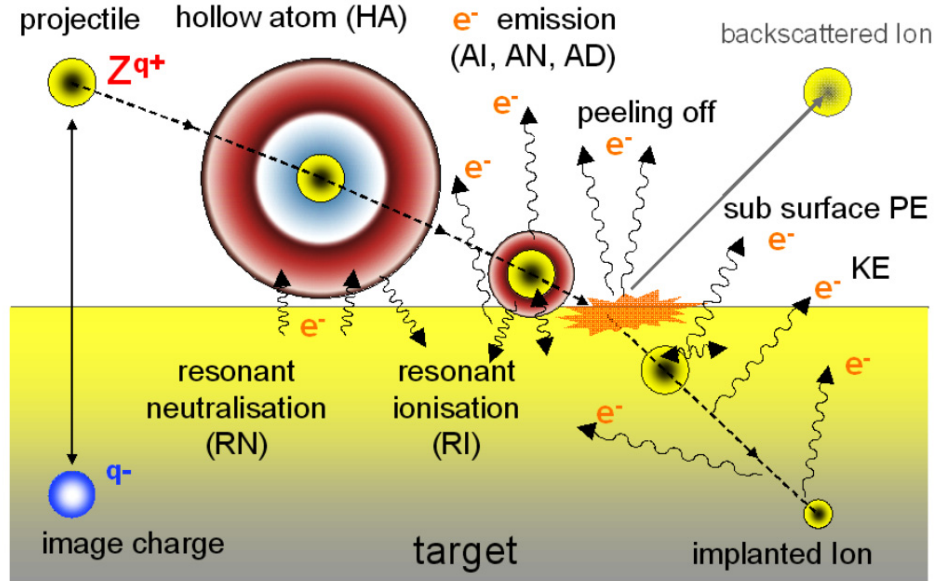
Figure 2.7: Overview of the different processes which take part during the impact of a HCI on a surface. Note the formation of a "hollow atom" and the different transmissions RN, RI, AN, AD and AI, which are of primary interest (cf. text) [20, p. 30].

Velocity Dependence of the Potential Electron Yield: For conducting materials, the COB model provides very good agreement with experiments [21, 38, 41, 86]. The experimental data is very well fitted by the empirically derived relation

$$\gamma_P(v) = \gamma_P^\infty + c_P^v \frac{1}{\sqrt{v}},\tag{2.27}$$

where γ_P^∞ is the velocity independent part of the potential electron yield mainly because of the "peeling off" of electrons at the target surface, and c_P^v is a free fit parameter. Because of the so-called image potential, very slow ions are highly accelerated towards the surface they collide with. This effect is represented by a natural upper limit of potential electron yields for minimal velocities [41]. For insulators and moderate impact energies (in the range of $20q$ eV $< E_{kin} < 100q$ eV) contradictory statements can be found in the literature. Meissl et al. [21, p. 75] measured the emission statistics for different projectile charge states and could successfully rule out effects concerning KE by subtracting the yields of different charge states. These results revealed that for insulators the PE seems to be nearly independent of the velocity of the approaching particle. Nevertheless, the functional dependence of the electron yield on insulators contains parts of the form $\frac{1}{\sqrt{v}}$ and this dependence could not be dropped in the fit functions but $c_{P,con}^v \gg c_{P,ins}^v$.

Incident-Angle Dependence of the Potential Electron Yield: It has been supposed that, basically, for conducting materials the PE only depends on the normal velocity

$v_\perp = v \cos\theta$ of the approaching ion towards the surface. Hence,

$$\gamma_P(\theta) = \gamma_P^\infty + c_P^v \frac{1}{\sqrt{v\cos\theta}} \tag{2.28}$$

$$= \gamma_P^\infty + c_P^v \frac{1}{\sqrt{v_\perp}}. \tag{2.29}$$

This assumption has been approved by various experiments [21, 27]. For insulators, to the contrary, no considerable angle dependence has been found in the same experiments which results in a very small fit parameter $c_{P,ins}^v$.

To explain this apparent discrepancy, theoretical calculations with a modified COB model have been done [96]. These simulations clearly underline, that the above surface part of the potential electron emission process plays a much less important role for insulators and, therefore, the emission is dominated by sub-surface processes. The argumentation in section 2.4 justifies the still high yields due to the larger mean free paths of excited electrons in insulators. Additionally, the calculated secondary electron yields of primary electrons excited by the impinging particle confirm these considerations [16].

The assumptions that insulating materials cannot provide enough electrons for high yields were proven to be wrong in experiments. Although for non-conducting materials the mechanisms that fill the emerged vacancies are relatively slow, enough electrons are at hand if projectiles hit yet untouched parts of the surface. It turns out to be clear that this often is the case if we consider, that there are about 10^{15} surface atoms per cm^2. Reasonable ion fluences for electron statistic experiments with HCIs are in the range of $10^8 \frac{\text{ions}}{\text{cm}^2\,\text{s}}$. This means, that for every impinging particle 10^7 surface atoms are available per second. An overview of the velocity and angle dependence of metals and insulators for PE and KE is given in section 2.6.

2.6 Summary of KE and PE on Metals and Insulators

From the above discussion it rapidly becomes clear that potential and kinetic emission follow individual rules which were fitted with empirical relations. Additionally, the fit constants differ for conductors and insulators. To emphasize the distinct response of conductors and insulators, research groups often chose Au as a good conductor and LiF as a wide band-gap insulator as sample materials. During the course of this master's thesis, borosilicat-glass (Duran) was also examined because it is used to manufacture the micro-capillaries used for ion-guiding [24]. Hence, electron emission yields from this compound where measured (cf. chapter 4). Table 2.2 gives a short overview of the velocity and the incident angle dependence of the total electron yield for conductors and insulators [21, 27, 36]. Other measurements also confirm these empirical dependencies [18, 44]. The understandings generated from this review show that potential electron emission of conductors is being driven almost fully by the perpendicular velocity and the potential energy carried by the highly charged ions, whereas for insulators the impact velocity hardly plays any role. The contributions of kinetic emission increase linearly

with the velocity and show a $\frac{1}{\cos\theta}$ angle dependence. The collected relations can be
written in one formula [20, p. 38]

$$\gamma_{tot}(v,\theta) = \gamma_P^\infty + c_P^v \frac{1}{\sqrt{v\cos\theta}} + c_K \frac{(v-v_{th})}{\cos\theta}\Theta(v-v_{th}), \qquad (2.30)$$

where v_{th} is the threshold velocity for kinetic emission (cf. section 2.3.1). For conductors we find a small γ_P^∞ and a high c_P^v, whereas for insulators it is the other way round. This concludes the summary over potential and kinetic emission from both, conductor and insulator surfaces. The next section 2.7 explains, how these emitted electrons can be detected in experiments.

	v dependence	θ dependence
PE	$c_P^v \frac{1}{\sqrt{v}} + \gamma_P^\infty$	$c_P^v \frac{1}{\sqrt{\cos\theta}}$
KE	$c_K \cdot v$	$c_K \frac{1}{\cos\theta}$

Table 2.2: Overview of the velocity dependence and the incident angle dependence of the total electron yield for conductors and insulators. The linearity of kinetic emission stops for high velocities where it saturates. It has to be noted that $c_{P,con}^v \gg c_{P,ins}^v$ and $c_{K,con} \ll c_{K,ins}$. Additionally the constant part of the electron emission yield γ_P^∞ is significantly higher for insulators. Overview of the velocity and angle dependence of γ. Data taken from [21, 27, 36]

2.7 Detection of Emitted Electrons Induced by Ions

From the previous sections, we know that electrons are emitted when neutral particles or ions hit a target surface. Apart from Auger de-excitation processes in the inner shells at the end of the impact, the energies of the emitted electrons are in the range of 0 to 100 eV. In this energy range it is not an easy task to detect the emitted electrons with
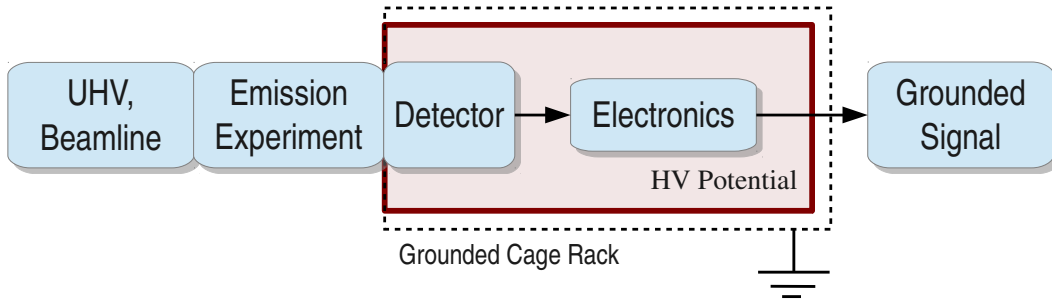

Figure 2.8: Schematic of the parts needed for the detection of emitted electrons. Note, that the detector and the processing electronics have to be inside the high voltage area. To ground the signal, a high voltage transformer can be used. An easier method is to carry the signal onto ground level by optical means (e.g. optical USB cable, cf. section 3.5).

a reasonably sized and affordable experimental setup. One possibility for high particle currents is the so-called current measurement (CM) method. Here, the impinging particle current is measured with a pico-amperemeter. Additionally an electron rejection cage is mounted around the target. On the one hand. if this cage is positively biased, the electrons emitted from the target are drawn away and the measured current at the target consists of both, the current of the incoming ions I_i and the current of the emitted electrons I_e

$$I_+ = I_i + I_e = I_i + \gamma \frac{I_i}{q}. \tag{2.31}$$

On the other hand, when the rejection cage is negatively biased, the emitted electrons are pushed back onto the target, and the measured current is equal to

$$I_- = I_i. \tag{2.32}$$

Hence, the total electron yield can be calculated to

$$\gamma = q \frac{I_+ - I_-}{I_-}. \tag{2.33}$$

A more complex, but also more sensitive method that also measures the EES (cf. section 2.8) is to focus and accelerate the electrons onto a semiconductor charged-particle detector. A high voltage (e.g. 30 kV) has to be applied at the detector in order that the electrons get enough kinetic energies to pass the entrance contact (approx. 12 μm aluminum for the Canberra detector and 500 Å boron implanted silicon for the Ortec detector) and to create sufficient electron-hole pairs in the sensitive layers of the detector. These electron-hole pairs can be detected, amplified and processed by an electronic detection system (cf. schematic shown in fig. 2.8). Before the signal is grounded all steps have to be done at high voltage. Hence, small components that fit into a high voltage cage of reasonable size are preferred. Such a compact detection system has been developed in the course of this master's thesis. A more profound and technical explanation can be found in section 3.5.

2.8 Statistics for Particle Induced Electron Emission

Particle induced electron emission is of great importance for sensitive particle detection or counting where particle currents become too small to measure with conventional methods (e.g. pico-amperemeters). Especially then, the statistics of the electron emission plays a crucial role. F. Aumayr and G. Lakits [29, 30] where among the first who correctly interpreted the electron emission statistics (EES) from clean gold under impact of slow (< 1 a.u.) heavy particles. If W_n is the probability for emission of n electrons

at a single impact event, the total electron yield γ is defined as

$$\gamma \equiv \bar{n} = \sum_{n=0}^{\infty} n W_n = \sum_{n=1}^{\infty} n W_n, \qquad (2.34)$$

$$\sum_{n=0}^{\infty} W_n = 1. \qquad (2.35)$$

It was commonly assumed, that the process of particle induced kinetic electron emission is a statistical process where a relatively small number n of mutually independent electrons out of a large ensemble of N electrons are excited inside the solid in a collision cascade that is initiated by the impact of the approaching particle. Hence, if the probability of a single electron ejection is p, a binomial distribution gives the resulting EES

$$P(n) = \binom{N}{n} p^n (1-p)^{N-n}. \qquad (2.36)$$

Moreover, for $p \ll 1$ and $n \ll N$, this binomial distribution converges to a Poissonian

$$P_n(\gamma) = \frac{\gamma^n}{n!} e^{-\gamma}. \qquad (2.37)$$

Following these considerations, one may fit a measured EES to a Poisson distribution, especially to calculate the probability for emission of no electron W_0 ("counting loss")

$$W_0 \approx P_0 = e^{-\gamma}, \qquad (2.38)$$

which becomes rather important for total electron yields in the order of unity. Apart from this, processes with zero electron emission can only be registered by time of flight (TOF) coincidence measurements. H. Winter [99] used this method to identify the counting loss at the threshold of kinetic emission, where γ is really small.

Additionally, it is long known, that PE processes follow a different statistics but careful experiments showed, that also for KE the classical Poissonian in eq. (2.37) does not hold true for small total electron yields. These deviations are ascribed to the fact, that the resulting collision cascades apparently do not involve a sufficiently large number of electrons inside the solid and, these electrons do not seem to be mutually independent. Furthermore, there is a non-negligible probability of electron backscattering from the detector which further deteriorates the spectra and has to be taken into account. F. Aumayr and G. Lakits introduced a new fit function [29,30], that corrects the defects of the Poisson distribution. They used a linear combination of normalized functions $F_n(E)$, which represent the respective emission events of n electrons per incident projectile,

$$S(E) = \sum_{n=0}^{n_{max}} C_n F_n(E), \qquad (2.39)$$

where the C_n are fitting parameters corresponding to the probabilities $W_n = kC_n$. The functions $F_n(E)$ themselves are composed of individual Gaussian peaks that constitute the backscattering of $m = 0, 1, ..., n$ electrons

$$F_n(E) = \sum_{m=0}^{n} P_n(m) f_n(E, m).$$

(2.40)

Here, $P_n(m)$ is the probability for backscattering m out of n electrons that arrive at the detector and $f_n(E, m)$ is a normalized Gauss function. For a more profound explanation with examples please refer to [30].

This concludes the theory part of this master's thesis. I tried to present a short overview of ion-surface collisions with special emphasize on electron emission. The processes for electron emission have been roughly divided into potential emission (PE) and kinetic emission (KE). Additionally, I tried to stress the differences between conducting samples and insulating samples. The next chapter 3 gives experimental details on the setup that was used in the course of the thesis at hand.

Chapter 3

Experimental Implementation

The previous chapter gives a brief overview of the theoretical concepts of ion surface interactions and the physical processes connected to it. Now, I will examine some of the experimental difficulties associated with the measurement of electron emission stimulated by impinging ions. Firstly, in section 3.1 the ion source will be explained in more detail. Next, section 3.2 shows how the ions reach the experimental chamber (section 3.3) and section 3.4 gives detailed information about the sample carrier. It illustrates where the samples were mounted, which materials were used and how they were prepared. Furthermore, sections 3.5 and 3.6 cast light on the detection system and the electronics needed to prepare and analyze the measured raw signal respectively. In the course of this master's thesis, a new ultra-compact setup for measuring ion-induced electron emission statistics was built and tested. The advantages of this new setup and some comparative thoughts can also be found in section 3.6. Summaries of problems I had with the high voltage (section 3.7) and the ultra high vacuum (section 3.8) conclude this chapter.

3.1   Ion Source SOPHIE

The compact Electron Cyclotron Resonance Ion Source (ECRIS, cf. section 2.1.1) SO-PHIE at the Augustin Laboratory of the Vienna University of Technology [64, 65, 104] was used to produce highly charged Ar ions up to charge states of $q = 11$ and in the energy range of $500q$ up to over $4000q$ eV. Typical Faraday cup currents are 500 nA for Ar^{1+} and a few pA for Ar^{11+}. Nevertheless, for EES detection with a surface barrier or a passivated implanted planar silicon (PIPS) detector (cf. section 3.5), where the ion current should not exceed the maximum counting rate of the detector and the electronics, Faraday cup currents of 1 pA are more than enough. Hence, the ion beam usually had to be attenuated to measure a spectrum. In fact, to be able to measure with the planar Silicon detector, the ion current had to be lower than the minimum of the measurement range of the picoamperemeters.

Figure 3.1 shows a schematic and a photo of the ion source, where a plasma is confined in a strong magnetic field created by four permanent magnet rings and a
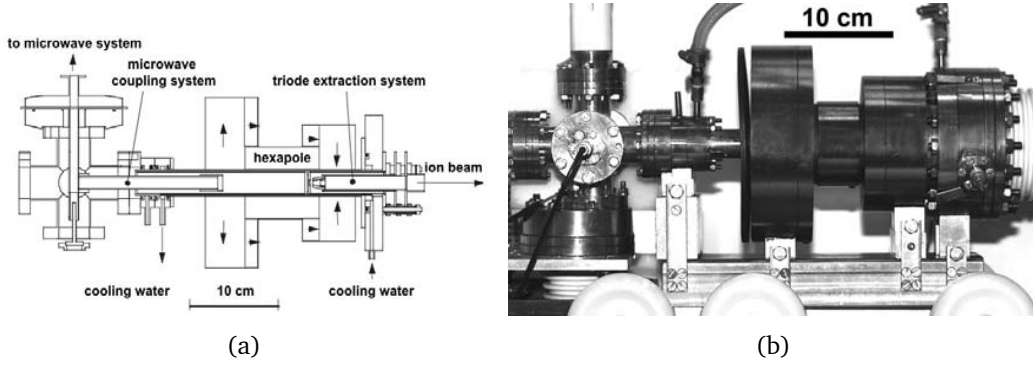
Figure 3.1: (a) Schematic drawing (top view; arrows show the direction of magnetization) and (b) photograph (side view) of a 14.5 GHZ all permanent magnet ECRIS (overall length about 40 cm) [65].

Halbach-type hexapole [105]. The pressure inside the source is of the order of 10^{-7} to 10^{-8} mbar. The electrons of the plasma are rotating around the magnetic field lines due to the Lorentz force with the angular frequency (or cyclotron frequency) $\omega_{ce} = \frac{eB}{m}$ where e is the elementary charge and m is the mass of the electron. Microwaves with the total power of up to 200 W in the frequency range of 12.75 to 14.5 GHz are transmitted from the microwave system at ground potential into the chamber by a travelling-wave tube amplifier and accelerate the electrons resonantly. In turn, the accelerated electrons ionize the gas particles step by step.

After the generation of the ions, they have to be extracted from the source by means of electrostatic fields (section 2.1.2). At the ion source SOPHIE, this is accomplished by a system consisting of 3 electrodes (an "Accel-Decel" extraction system) to be able to hold back the electrons inside the ionization chamber. This triode was optimized for low acceleration voltages between 1 and 6 kV. Finally, the ECRIS can be fully controlled and remotely operated by a computer connected via Ethernet. A thorough description of the ion source can be found in [64].

3.2 Beamline

This section provides information on how the extracted ions travel through a beamline to the sample carrier that is located in the target chamber. Magnetic and electric fields focus and guide the ion beam to its destination. A schematic of the used beamline is shown in fig. 3.2. Directly after the extraction from the ECRIS, the ions are focused by two magnetic quadrupoles. It is important, that a magnetic quadrupole only focuses the beam in one direction, but defocuses it in the perpendicular direction. A focussing net effect is reached only if two magnets are used. Then a sector magnet selects particles with a certain charge to mass ratio

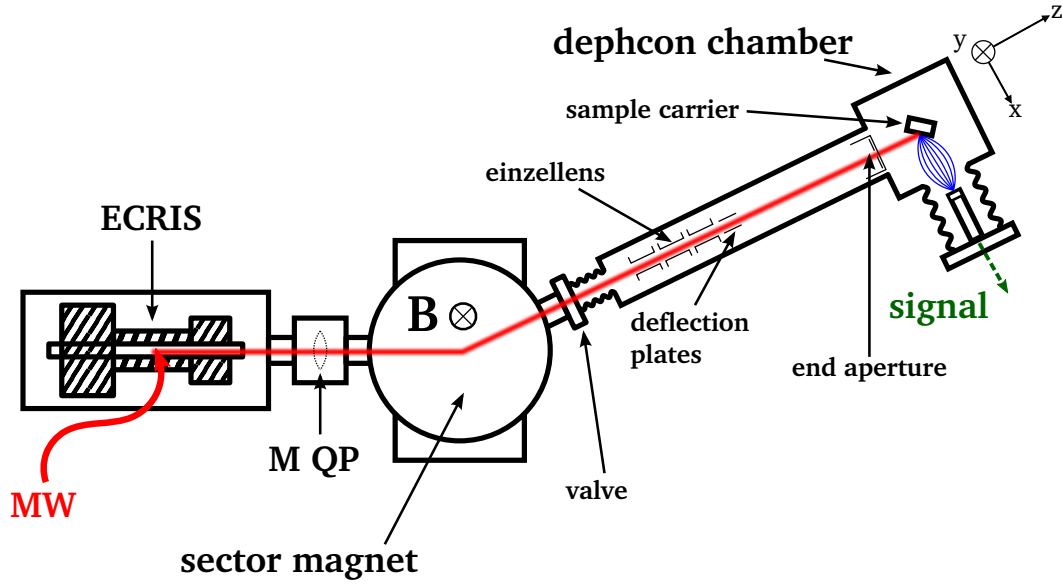$$\frac{q}{m} = \frac{2E_{kin}}{r^2 B^2},\tag{3.1}$$

Figure 3.2: Schematic of the most important elements the ions pass on their way to the sample. Directly after the extraction from the ECRIS pumped by microwaves, the ions are focused by two magnetic quadrupoles (M QP). Then a sector magnet selects particles with a certain charge to mass ratio and guides them into the beamline where they are focused by an einzellens. Deflection plates steer the beam so that it passes the end-aperture, enters the Dephcon chamber (section 3.3) and hits the target (section 3.3).

where E_{kin} is the kinetic energy of the ions and r is the radius of their circular motion in the magnet field B of the sector magnet. The particles with the corresponding charge to mass ratio are guided into the beamline.

The actual beamline mainly built with stainless steel tubes with a diameter of 10 cm is separated from the magnets by a vacuum valve. A Faraday cup is positioned directly before this valve. It can be driven into the beam to measure the incoming ion current and record detailed charge to mass spectra. This Faraday cup is very important to be able to select the right ions from the large amount of charged particles extracted from the source. This is done by comparing the position of the peaks corresponding to different charge to mass ratios. Nevertheless, sometimes it is very hard to adjust the current of the sector magnet in order that the desired ion species enters the beamline. During operation, a 1.5 cm aperture mounted directly above the Faraday cup defines the maximum diameter of the beam.

Before the ions hit the sample (cf. section 3.4) they are focused again by an einzellens located approximately 30 cm after the valve at the entrance. An einzellense is a charged particle lens that focuses without changing the energy of the beam. It consists of three cylindrical tubes arranged along an axis that are biased symmetrically so that the ions regain their initial energy upon exiting the lens. Deflection plates are attached at the end of the third tube to steer the beam so that it passes the end-aperture and enters the Dephcon chamber (section 3.3). Figure 3.3 shows a drawing of this lens system. The 3 cylindrical tubes and the deflection plates are electrically isolated. All electrodes
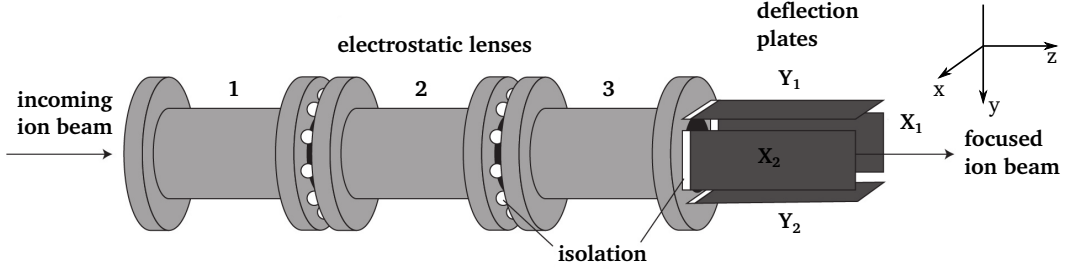
41

Figure 3.3: Drawing of the electrostatic einzellens with attached deflection plates [59, p. 3]. All electrodes are electrically isolated. Note the label of the deflection plates and the definition of the direction of the axis.

can be put at different potentials to achieve the required focus and deflection. They are connected to the power supplies via a multipin feedthrough situated above the lens. Typical operation voltages are 0 V or ground level for cylinders 1 and 3, +300 V for the second cylinder in the middle and 0 up to ±40 V at the deflection plates. To minimize the aberration of the deflection plates they should be biased symmetrically, e.g. $X_1 = +20$ V and $X_2 = -20$ V (deflection towards the right).

Directly before the chamber where the sample is located, the electron repeller and the end-aperture are situated. The beam limiting aperture (end-aperture) has a diameter of 1 mm and a distance of 12 cm from the center of the target chamber. To be able to optimize the beam parameters, a picoamperemeter measures the current deposited by the impinging ions on the end-aperture. More information on the beam limiting components and the electron repeller can be found in the next section 3.3.

A reasonably low pressure is needed throughout the whole beamline to avoid neutralization of the ions on their way to the sample. In these experiments, a maximum pressure of the order of 10^{-8} mbar is guaranteed but most of the time it was considerably lower (10^{-9} mbar and mid 10^{-10} mbar region). I had a lot of serious trouble getting acceptable low pressure. Hence, I decided to dedicate some considerations to the vacuum system and the problems associated with it. This discussion can be found in section 3.8.

3.3 Dephcon Chamber

The Dephcon chamber [106] is a small and portable device with an integrated EES detector. The name dates back to its initial purpose: the detection of electrons for phase control of pulsed lasers. A true to scale cut of the Dephcon chamber can be found in fig. 3.4. The ion beam enters the target chamber from the right and passes the end-aperture (diameter = 1 mm, 12 cm distance from the target) and the electron repeller (a cylindrical tube with a 3 mm orifice and 10 cm distance from the target). The end-aperture is the last beam limiting component before the ions hit the sample. It is connected to a picoamperemeter to measure the deposited charge of the incoming ions. This is very important to adjust the beam by modulating the sector magnet current and
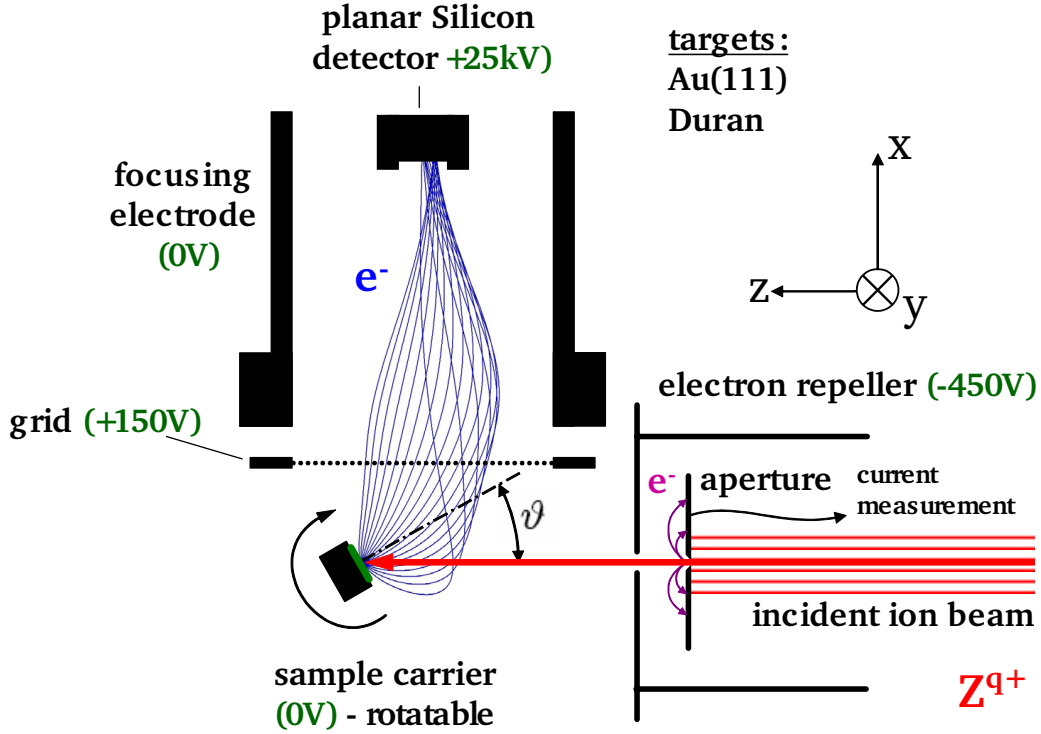
Figure 3.4: A true to scale cut of the Dephcon chamber [20, p. 61] (consult [106] for detailed dimensions). The electron repeller and the end-aperture are also shown.

the potentials of the einzellens and the deflection plates. It was also used to measure spectra of the charge to mass ratio of the ions inside the beamline (cf. section 3.2).

The electron repeller is biased at negative voltage and has two purposes. Firstly, it repels the electrons created at the end-aperture back into the beamline and away from the detector. This greatly reduces the undesired electron background measured at the detector. Secondly, it helps guiding the electrons emitted from the target (the electrons we want to detect) towards the grid and the detector. The grid is a highly transparent mesh made of a thin wire. It is located directly in front of the grounded tube surrounding the detector. This tube acts as detector protection and focusing electrode for the electrons. The transparent grid is put at positive voltage to attract the electrons emitted from the target located at the rotatable sample carrier (cf. section 3.4). The end-aperture, the electron repeller and the transparent grid are connected to their power supplies or amperemeters by a feedthrough situated directly above the electron repeller.

The key part of the Dephcon chamber is the planar silicon detector (cf. section 3.5). It is put at high voltage and mounted on a flange connected to an insulator (cf. fig. 3.5). The grounded focusing electrode additionally protects the detector from arcing and similar effects due to the applied high voltage. The master's thesis of M. Simon [20] gives very detailed information about the dephcon chamber. It also presents ray-trace simulations with SimION performed for the particular extraction geometry calculating the
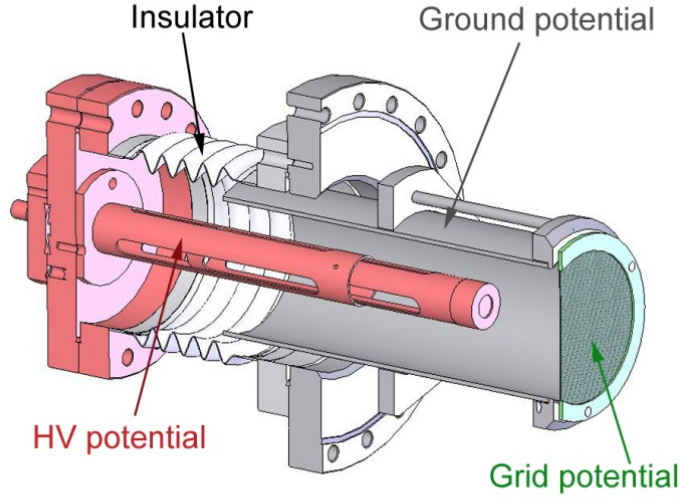
Figure 3.5: The planar silicon detector mounted on the insulator flange of the UHV setup. The parts held at high voltage are drawn in red [21, p. 45].

electron paths from the target to the detector. The simulations assure that the applied extraction field (typically about 100 V/cm) is sufficient to collect all electrons with energies below 50 eV emitted into the half solid angle above the target and detection efficiency factors are discussed for electrons with higher energies. Note, that the detection efficiency (mostly denoted ϵ) strongly depends on the potentials of the grid and the electron repeller as well as on the sample carrier position and rotation angle. Furthermore, new experiments (cf. [107]) clearly indicate that ϵ deteriorates towards ultra-low ion impact velocities ($E_{kin} < 10$ eV). This is mainly because to reach this range of impact energy, the target has to be biased.

Finally, the vacuum pressure in the chamber was of the order of 10^{-10} mbar if the beamline was closed (no measurement possible) and it rose to about $1 - 2 \cdot 10^{-9}$ when the valve towards the magnet was opened. Additionally, no measurements were possible if the pressure gauge and the ion pump at the Dephcon chamber had been activated. This is due to the high number of electrons and photons emitted from these sources that are detected and that distort the spectrum.

3.4 Sample Carrier

The sample carrier is one of the most important devices used in an experiment. For the measurements in the Dephcon chamber, the carrier had to be reasonably small so that it did not significantly deteriorate the electric field lines created by the grid and the electron repeller and used to capture the emitted electrons. Moreover, it should

be apt to hold more than one sample because opening the vacuum chamber and the subsequent pumping and heating process need a lot of time. Lastly, at least one of the samples should be heatable to remove surface impurities.
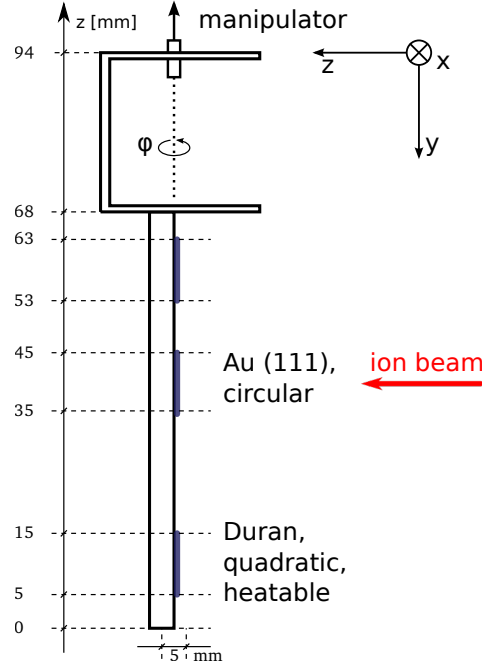

Figure 3.6: Side view of the sample carrier used in the course of this master's thesis. The ions hit the targets (AU(111) and Duran) from the right. The sample carrier is mounted on a $xyz\varphi$-manipulator. It has a width of 11 mm and a depth of only 5 mm. The bottom sample is heatable.

All these requirements are met by the sample carrier shown in fig. 3.6 that was used during this master's thesis. It can hold 3 different targets of about 1 cm^2 size. The sample carrier is relatively small and offers a heating wire with a maximum heat output of 8 W for the bottom slot. With this power, an approximate maximum temperature of 400 °C can be reached but this is not necessary for cleaning the target. The carrier is mounted on a xyz-manipulator and can be rotated. It has a width of 11 mm and a depth of only 5 mm. The sample carrier is electrically insulated. Four feedthroughs for the target, the heating and a thermocouple to measure the temperature of the heatable sample were installed.

3.4.1 Examined Target Materials

Only 2 of the 3 target slots were used. On the position in the middle, a circular AU(111) single crystal target with an approximate diameter of 8 mm was mounted. Gold is one of the best-researched conductors and a lot of experimental data to compare with exists. Especially in our group, many EES measurements on gold were done [27,36,38]. In the course of this master's thesis a new compact electron emission setup was built. Hence,

45

I used the gold target to test the new setup and to compare new data with already measured total electron yields.

The second target at the bottom was a square piece of borosilicate glass (Duran) and had a size of 1 cm^2. Duran mainly consists of SiO_2 (81%) and B_2O_3 (13%). It has a transition temperature T_g of 525 °C and its absorption of light in the spectral range from about 310 to 2200 nm is negligibly. The Duran Group® provides very detailed information on the properties of this type of borosilicate glass on their web page [108]. The bulk and the surface conductivity of Duran glass exponentially depends on the temperature (see section 4.6 and [14, 109]).

Borosilicate glass has been recently used to build macro sized glass capillaries that guide HCIs without changing their charge state [12, 13]. This recently discovered effect is based on a self organized build up of charge patches along the inside of the capillary. These charge patches deflect the incoming ions and allow them to pass through the capillary. It is very interesting to examine the electron emission from this material because the knowledge could give important information on the ion-surface interaction and the formation processes of the charge patches. Due to the exponential dependence of the conductivity of Duran glass on the temperature, the guiding effect can be controlled by modest variations of the capillary temperature.

3.4.2 Preparation of the Target Surfaces

Reproducible and convincing experiments require a clean and well defined target surface. To be specific, the surfaces of the samples have to be prepared for the measurements and many different target preparation methods exist. For conductors, one of the most important method is sputtering the surface with a huge number of singly or doubly charged Ar ions. To prepare the surface of the Au(111) sample a beam of 1000 keV Ar^{+1} ions with a current of approximately 6 nA on the target was directed on the gold surface to remove the impurities. The whole sample surface was irradiated for at least half an hour before EES data was measured.

Sputtering is not very efficient for insulators because deposited charge is not conducted away. Therefore, I had to anneal the Duran sample at 100 °C to 150 °C to remove the impurities on the surface. Moreover, the Duran had to be heated during the EES measurements because electron emission strongly depends on the charge deposited at the position of the ion impact. To conduct away enough charge so that accurate measurements are possible a target temperature of about 100 °C is necessary. W. Meissl [21] provides more information on the heating of insulators during EES measurements and some temperature dependent yield measurements.

3.5 The Semiconducting Planar Silicon Detector

When a HCI hits the surface of the target all different sorts of particles are emitted. We are interested in the electron emission and want to detect as many electrons as possible (electron detection efficiency ϵ). Apart from Auger de-excitation processes in the inner

shells at the end of an ion impact, the energies of the emitted electrons are in the range of 0 to 100 eV. Indeed, the majority of the electrons has very low energy below 40 eV. To measure the EES distribution during ion-surface interaction usually these slow electrons emitted from the interaction region are extracted by a weak electric field through a highly transparent grid and accelerated onto a planar Silicon type detector biased at +25 kV (cf. section 3.3, especially fig. 3.5). A great part of the information about the detector presented in this section can be found in the detector section of the Ortec product catalog [110].

Charged particle detectors are basically reversely biased diodes with parallel planar electrodes. Two different kinds of this type of detector are commonly used. The surface barrier detector on the one hand, has thin metal contacts as electrodes. On the other hand, the surfaces of the passivated implanted planar silicon (PIPS) detector are doped by ion implantation. The detector in the dephcon chamber is a PIPS detector from Canberra (BKPD100-12-300AM). Impinging electrons create electron-hole pairs that are captured by the electric field of the bias voltage (typically 45 V) and gather at the electrodes. There they are measured as accumulated charge and further processed by the data acquisition electronics (cf. section 3.6). The number of the created electron-hole pairs is proportional to the energy of the impinging electron. This is precisely the energy the electrons gain due to the bias voltage applied at the whole detector (e.g. 25kV) when they are accelerated towards it. The production of one electron-hole needs approximately 3 eV.
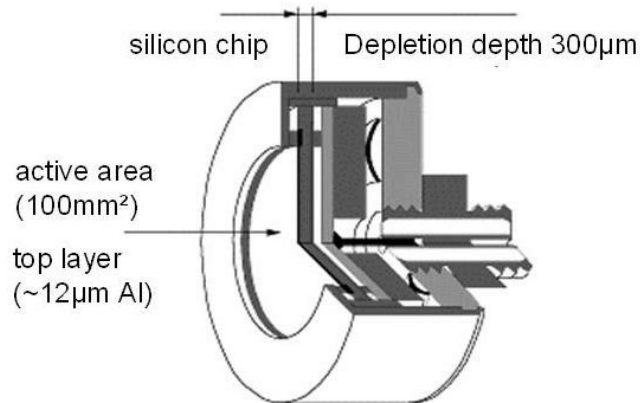

Figure 3.7: Design of the Canberra planar surface barrier detector [20, p. 70].

Planar silicon type detectors are characterized by their active area and their active thickness, where electron-hole pairs can be created. The installed detector from Canberra (BKPD100-12-300AM, cf. fig. 3.7) has an active area of 100 mm^2 and a minimum depletion depth of 300 μm. The depletion depth depends on the detector type and the bias voltage (it increases with applied bias voltage). The length of the depletion depth is of great importance so that impinging particles can deposit all of their energy before leaving the diode. For example, a depletion depth of 300 μm is sufficient to collect the

energy of a 250keV electron. In this setup, the electron only have an energy of 25keV. Hence, we can safely assume that the whole energy is deposited in the active region of the detector.

The size of the active area is of significance because as the area increases, the efficiency but also the noise of the detector increase and consequently the energy resolution decreases. Due to the planar and parallel electrodes, the detector has a specific capacitance of the corresponding parallel-plate capacitor that is directly proportional to the sensitive area and indirectly proportional to the depletion depth. For a 300 μm depletion depth the capacitance is of the order of 0.4 pF/mm^2. Thus, the approximate capacitance of the Canberra detector is 40 pF. This is relevant because the preamplifier has to be chosen correspondingly (cf. section 3.6) and it affects the energy resolution of the detector which is of uttermost interest. In general, we find that the higher the capacitance, the higher is the noise and the lower is the resolution. Another quantity that influences the energy resolution is the so-called leakage current. This is a small current that is conducted through the diode although it is reversely biased. It depends on the temperature and the detector type and is directly proportional to the electronic noise. Another aspect, that influences the energy resolution of surface barrier detectors is the electrode where the bias voltage is applied. This is a 12 μm aluminum layer for the used Canberra detector. The electrons already lose part of their energy when they trespass this dead region. The total energy resolution for the Canberra detector is about 6.9 keV.

In addition to that, every detector has a specific signal rise-time. This quantity together with the signal processing electronics defines the number of impact events that can be recorded per second or time step. For a planar silicon detector the rise-time is of the order of $W \cdot 10^{-7}$ s, where W is the depletion depth measured in mm. Thus, the installed Canberra detector has a rise-time of approximately $3 \cdot 10^{-8}$ s. Nevertheless, the time resolution of the detector is only of the order of 10^{-6} s [20, p. 70]. This limits the ion current that can be analyzed. Above a rate of about 15 kHz a non-negligible part (more than 1 %) of the incoming pulses starts to interfere. This leads to a so-called pile-up of impact events.

However, the large resolution time also assures that all electrons emitted due to a single impact event reach the detector within its resolution time. Consequently, the n electrons emitted due to a particular ion impact will be registered as one impact with an energy of n times 25 keV rather than n individual 25 keV electrons. The number of electrons emitted in a particular ion-impact event can therefore be deduced from the pulse height distribution of the detector. More details on this ES detection method and its appropriate evaluation can be found in [29, 30, 33, 53–55] and references therein.

Electrons that hit the sensitive area of the detector lose energy by Coulomb interaction with the electrons of the absorbing materials creating electron-hole pairs. Because of their light mass, they are so intensely scattered that their trajectory in the material is a jagged line and even backscattering may occur [30]. Although, the backscattered electron presumably returns to the detector it has to trespass the dead layer not only 1 but 3 times. As a result, it only deposits a part of the 25keV in the active region lead-

ing to a lower measured energy and a broadening of the peak. For large total electron yields γ the different peaks cannot be resolved and a broad large peak that is shifted to lower energies is observed (cf. fig. 3.8). This effect has to be taken into account when analyzing the pulse height spectra [20, p. 73].

Lastly, a planar silicon detector is very delicate and sensitive to radiation damage. This can be a problem while heating the vacuum chamber, when field emission occurs due to the high voltage or when the ion beam is too intense. The symptoms are a high leakage current resulting in a higher detector noise. In that case, peak broadening or even double peaking are observed. The threshold dose for electrons is of the order of 10^{13} electrons per cm^2.

This concludes the section about the installed planar silicon detector from Canberra. I hope that it emphasizes the importance of the choice of the right detector and presents the key information in a well-structured way. The next section 3.6 gives an account of the new processing and data acquisition electronics that is needed to analyze the signal.

3.6 Processing and Data Acquisition Electronics

In this section I want to explain how the accumulated charge at the detector electrodes is amplified and prepared for the measurement software. I would like to emphasize the advantages of the newly built electronic setup and why the built in components had been chosen. In most energy spectroscopy applications a preamplifier prepares the signal to be processed by a shaping or spectroscopy amplifier. This amplified signal is then pulse height analyzed and sorted into a histogram by a multichannel analyzer (MCA). In essence, the next paragraphs describe exactly, how an energy spectrum is accumulated. It is important to realize, that all steps taken before the grounding of the signal have to be done at high voltage. Hence, small components that fit into a high voltage cage of reasonable size are preferred.

Preamplifier: The first and probably most important component of the detection electronics is the preamplifier that extracts the signal from the detector without significantly degrading the intrinsic signal-to-noise ratio. This means, that it should be connected as close as possible to the detector. For energy spectroscopy with a planar silicon detector, a charge-sensitive preamplifier is the preferred choice. It integrates the signal accumulated at the detector electrodes on a feedback capacitor so that its output signal height is directly proportional to the charge created in the detector ($V_{out} \propto Q_D$). The size of the feedback capacitor has to be adjusted to the capacitance of the detector.

Spectroscopy amplifier The next part of the electronics is the spectroscopy amplifier. It prepares the signal to be pulse height analyzed and offers pulse-shaping controls that are crucial for optimizing the performance and the resolution of the analog setup. It usually produces a very accurate output signal representing the energy deposited in the detector at the cost of time resolution. In the event that two or more pulses reach the

amplifier within its resolution time, the output signal cannot be used. Usually, a second device (e.g. a fast timing amplifier) with a very fast but inaccurate output is installed to prevent this pulse pileup. Different pulse shaping techniques exist to form the output signal (e.g. semi-Gaussian pulse shaping, cf. [110]). To ensure good energy resolution at high counting rates the dc-coupled high-end spectroscopy amplifiers need a baseline restorer. This device cancels the dc offsets of the earliest stages that would be magnified otherwise.

Multichannel Analyzer (MCA)   The MCA analyzes the stream of voltage pulses from the spectroscopy amplifier and sorts them into a histogram of pulse-height versus number of events (e.g. the x-axis represents the pulse height or number of electrons and the y-axis the number of registered events). This is then called an energy spectrum. Recently, at PC based systems, the MCA is replaced by a small hardware component called the multichannel buffer (MCB) and a software application that processes the data.

A sample spectrum of a measurement campaign in the "Forschungszentrum Dresden" [107] can be seen in fig. 3.8. Very slow Xe^{20+} ions are directed onto lithium fluoride (LiF) with an approximate electron yield γ of 40 electrons. We can see that the electron yield is a statistical quantity (the number of emitted electrons statistically varies). Furthermore due to electron backscattering in the detector, the single peaks (e.g. 38 electron, 39 electrons, etc.) are broadened and only one large peak shifted to lower energies is observed. Then, we can identify a second, even larger peak at a very low number of electrons. Electronic noise and field emission contribute to these events that greatly deteriorate the spectrum. Nevertheless, because of the lower level discriminator (LLD) of the spectroscopy amplifier no events are recorded below a certain threshold. Pileup is not observed partly because of pileup-rejection and a low count rate.

3.6.1   Conventional setup with NIM crate

A schematic of the usual EES setup can be seen in fig. 3.9. It was developed and used by Meissl et al. [16, 21] and involves a standard charge-sensitive preamplifier (Ortec 142B) with a short connection (via a coaxial vacuum feed through) to the planar silicon detector. Both of them are at high voltage and therefore surrounded by a grounding cage. The preamplifier output is lead via a high voltage secure tube to a second cage that is also operated at HV potential. It includes a NIM crate containing the spectroscopy amplifier Ortec 570 and the Ortec 926-M32-USB multichannel buffer (MCB) with USB output. The Spectroscopy amplifier produces a signal with a pulse height proportional to the number of electrons simultaneously impinging on the detector and the MCB digitizes and sorts these pulses into a histogram. Finally, the prepared pulse height spectrum is transferred to the measurement computer via an optical USB cable that can be linked directly to ground potential. Additionally, a battery pack is located in the rack to provide the bias voltage for the detector. The cage also has to contain a heavy high-voltage-proof transformer, which powers the NIM crate. In this setup high voltage
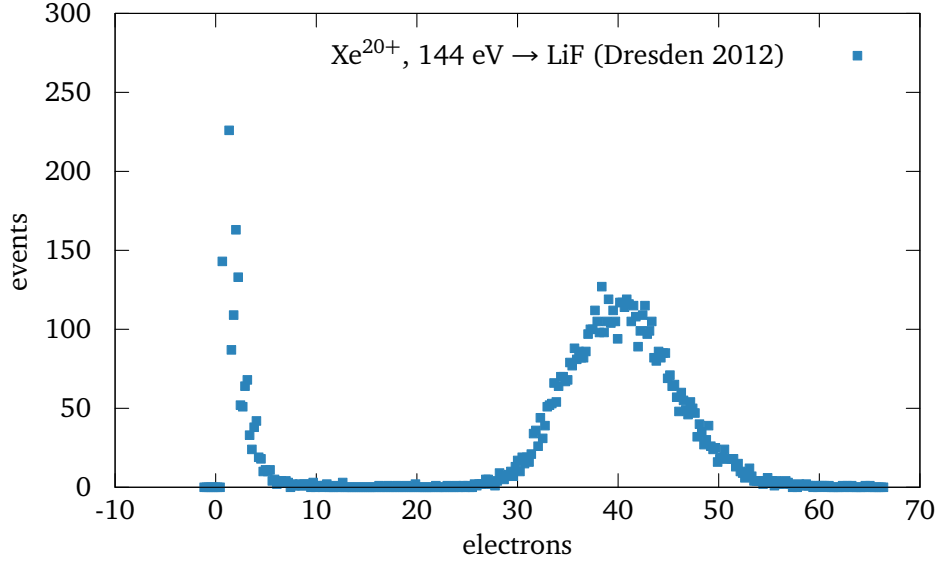
Figure 3.8: Sample spectrum of a measurement campaign in Dresden. Very slow Xe^{20+} ions are directed onto lithium fluoride. The electron yield γ is approximately 40 electrons [107].

has to be applied at two parts, the area at the planar silicon detector and the rack with the NIM crate. These parts are linked with a tube that is also put at high voltage.

3.6.2 New setup

We have now designed and constructed a novel, light and compact electronics replacing this heavy and bulky equipment by small and light components, which can be operated using battery packs only. Even the pulse height analysis is now performed at high voltage and just the resulting pulse height spectrum is communicated by optical fibers to the measurement PC at ground potential. A schematic of the new electronics is shown in fig. 3.10. The signal dependent on the charge accumulated in the detector by impinging electrons is now preamplified by an Amptec **A250 charge-sensitive preamplifier** chip mounted on a test board (PC250). The most important reason for choosing the A250 is that it can be used together with a wide range of detectors because the installed field-effect transistor (FET) can be matched to the particular detector capacitance. The noise performance of the A250 is such that its contribution to the FET and detector noise is negligible. It is essentially an ideal amplifier in this respect.

The output of the preamplifier is subsequently processed and digitized by the **digital pulse processor DP5** also from Amptec. The DP5 replaces both the shaping amplifier (Ortec 570) and the MCA system in the previous analog spectroscopy system (cf. fig. 3.9). An analog prefilter circuit prepares the signal for a 12-bit analog-to-digital converter (ADC) for accurate digitization. Then the digital pulse shaper processes the ADC output continuously generating a real time shaped pulse. There are two parallel signal processing paths inside the digital pulse processor (DPP), the "fast" and the "slow"
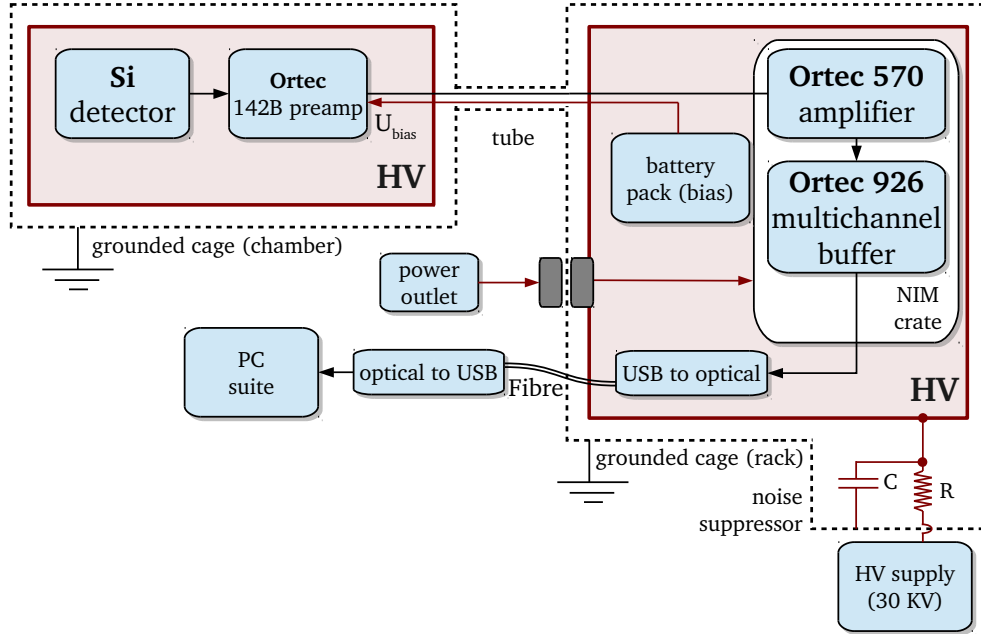
51

Figure 3.9: Schematic of the bigger EES detection electronics developed and used by Meissl et al. [16,21].

channel. The "slow" channel is optimized to create accurate pulse heights whereas the "fast" channel obtains timing information. Then a pulse selection logic rejects or accepts the received pulses (pile-up rejection, risetime discrimination, etc.). Consequently, the accepted pulses are stored in a histogram memory and transferred via a USB cable to a free (!) software interface from where the pulse processor can be controlled and the spectrum can be viewed and saved.

The circuit boards of the A250 and the DP5 are both mounted in the same small electronic housing, that is shown in fig. 3.11. For galvanic insulation the prepared signal is transferred to the measurement computer at ground potential via a **fiber optical USB cable** (Opticis M2-100). Since the power consumption is drastically reduced compared to the previous setup, instead of an HV-proof power transformer two small **battery packs** are sufficient to provide the detector bias voltage (45 V) and the power (+5 V and ±6 V) for operating the preamplifier and the digital pulse processor unit for a period of at least a whole day. A special charge unit is used to recharge the batteries used for the pulse processor and the preamplifier. A Heinzinger power supply was used to provide the high voltage (for the exact model cf. section 3.7) and a low-pass filter consisting of a resistor and a capacitor was added to reduce the high frequency noise (cf. fig. 3.10).

It rapidly becomes clear, that the compact design facilitates the handling of the high voltage areas as well as the construction and the operation of the detection system. Firstly, the compact design allows all the components, that have to be operated at high voltage to be placed in a single HV cage directly mounted at the flange of the detector.
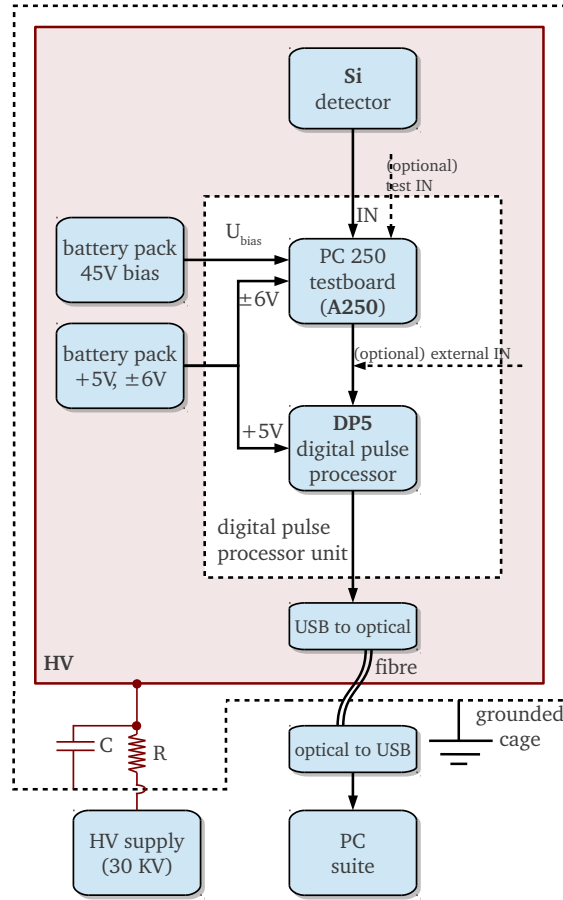
Figure 3.10: Schematic of the new compact EES detection electronics developed in the course of this master's thesis.

This greatly reduces the intrinsic noise of the detection setup and allows the accumulation of very accurate energy spectra. Secondly, since fewer components have to be put at high voltage and both power and signal are no longer transmitted through analog transformers, the risk of arcing and high voltage discharges is drastically reduced. Hence, the life-time of the mounted electronic parts and especially the life-time of the preamplifier are increased. Thirdly, the DPP also offers several other advantages including a delta mode, improved performance (higher resolution, higher throughput), flexibility, versatile and free software, lower power consumption and small size. Finally, not only the compact design but also the low cost of the new measurement electronics, might allow other groups to easily employ the EES technique at their beamlines and use it for diagnostic purposes [53–55], surface structure analysis [56,57], or basic ion-surface collision studies.
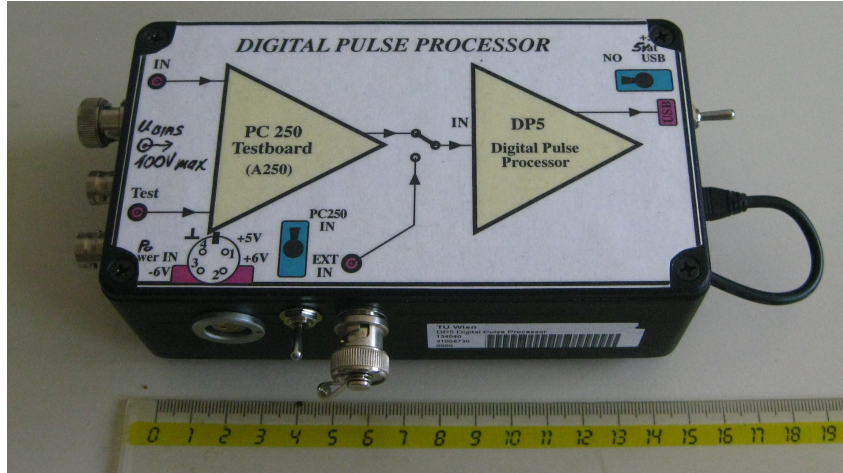
Figure 3.11: Photo of the key part of the new detection electronics, where the digital pulse processor DP5 is built in. Inputs are the signal from the preamplifier (IN), the bias voltage from the battery pack (U_{bias}), the power input (Power IN), a test input (Test) and an optional external input (EXT IN) if another preamplifier wants to be used. A switch defines if the power for the pulse processor comes from a battery pack (normal usage) or from the USB cable (this is not possible for a fiber optical cable). The only output is the USB-out, which is not visible. The ruler shows that the digital pulse processor unit only has a size of approximately 15 cm.

3.7 Problems with High Voltage

The detector and the connected electronics have to be put at high voltage so that the accelerated electrons gain enough energy to compensate the statistical error of the detector (energy resolution, ≈ 6.9 keV). However, different problems arise when the ideal operating voltage of 30 kV is applied.

In the first place, the power supply has to provide a very stable and noise-free common potential for the measurement components. I used two different power supplies (the newer Heinzinger PNC 30000-5ump and the older Heinzinger HNCs 30000-5neg) that both had a maximum potential of 30 kV. Since this is already the preferred operating voltage they were driven at their limits. This lead to high frequency noise at the Heinzinger PNC 30000-5ump rendering the measurements impossible. With this in mind, we realize that the choice of a suitable power supply is a very important one. Furthermore, I added a low pass filter between the power supply and the measurement electronics inside the cage (cf. fig. 3.10) that greatly reduced the high frequency noise. This filter consists of a resistor (Vishay RW30/305, 300 kΩ, maximum load 480 W) and a high voltage capacitor (2000 pF) suited for 30 kV.

Secondly, the grounded cage had an approximate size of $50 \cdot 30 \cdot 30$ cm^3. Although every component held at high voltage had a distance of at least 10 cm from the cage some disturbing noise and small sparks due to high voltage discharges were created at some places and especially at corners. Consequently, the measured spectrum was deteriorated. These edges had to be treated with sandpaper and they had to be cleaned.

Thirdly, it is of great importance to correctly ground the electronics. This means, that all grounded parts and even more important, all electronic components held at high voltage (common potential) should each have a common ground (e.g. one place where the cables are connected). This minimizes the probability of so-called earth loops and hence, the noise. I measured the total count rate of the electronics when there was no real signal (no electrons etc., this represents more or less the noise level) and optimized the place inside the cage where the cables should be connected. It turned out, that the most suitable place is the detector flange itself.

Not only the noise created outside the measurement chamber but also field emission and high voltage discharges inside the vacuum chamber greatly distorted the measured spectrum. Especially after opening the vacuum chamber, field emission became a serious problem. After applying a potential of 30 kV for some time (e.g. 5 minutes), the detector started to measure an innumerable amount of electron and photons. Then, even the pressure in the chamber rose directly proportional to the applied voltage, sometimes even by a factor of 10. This is a serious problem that depends on the number and sizes of the microscopic corners and edges of the components inside the chamber which are held at high voltage. Another contributing factor seems to be the amount of dust particles that had accumulated in the detector flange. We could significantly reduce the amount of noise by cleaning the affected parts with CO_2. Moreover, at some point we noticed that the highly transparent grid had been damaged slightly. The protruding wires can then lead to a Corona discharge. With this in mind, we opened the experiment chamber and fixed the grid. Indeed, this greatly reduced the background signal and the problems with discharges.

On the other hand, the quality of the insulator also plays an important role. Again, treatment with sandpaper, careful cleaning and electropolishing minimize the effect of field emission. Additionally, conditioning at high voltage helps to burn off small edges and to reduce the perturbations, but it also might damage the detector (cf. section 3.5, radiation damage). Given these points we reduced the operating Voltage from 30 kV to 20 or 25 kV. This does not significantly deteriorate the resolution but greatly reduces the problems with high voltage. The purpose of these considerations is to call attention to these different problems. I hope, that future experiments can benefit from this description.

3.8 Vacuum technology

Experiments involving ions or electrons that travel along macroscopic distances need to be undertaken at ultra high vacuum (UHV) in order that the charged particles are not neutralized on their path along the beamline. Given, that I had a lot of problems to create a good enough vacuum to conduct measurements, I want to spend a few words on this topic. A very good introduction to vacuum technology is given in the catalog of Pfeiffer [111].

The beamline consists of screwed Conflat (CF) flanges of different dimensions with a leak rate of $< 1.0 \cdot 10^{-11}$ mbar and can be baked up to 450 °C. The vacuum is created

by different vacuum pumps mainly characterized by their throughput (gas or pV flow) and pressure ranges. The pumps installed on the beamline were a Turbomolecular pump (Hipace 80 from Pfeiffer with a pumping speed of $S \approx 66$ l/s) and two ion getter pumps (Titan Ion Pump from Gamma Vacuum with a pumping speed of $S \approx 480$ l/s). Detailed information on the pumps and the vacuum system used in the Augustin laboratory can be found in the project report of E. Gruber [112]. Only some important aspects regarding the experiment will be outlined here.

It is vital, to keep the equipment that will be mounted inside the vacuum chamber clean and free of oil. Furthermore, desorption of gas particles with a time constant of approximately 1 hour from the walls leads to difficulties during the pumping process. The reason is that residual gas (mostly water) is adsorbed to the chamber walls and the vapor pressure from water is too high to reach ultra high vacuum (UHV). Especially the light elements are hard to get rid off. **Baking out** the vacuum chamber at temperatures higher than a 100 °C increases the desorption rate during the pumping process and significantly lowers the end pressure that can be reached. From the experience I made during the work on this master's thesis, a bakeout temperature of 145 °C for at least 3 days is sufficient to get an end pressure of the order of 10^{-10} mbar. Moreover, the gas particles do not behave very intuitive at very low pressures. Keeping this in mind, long narrow tubes with a low "conductivity" may lead to unexpected end pressures (this is used for differential pumping).

Equally important is to make sure that there are no leaks in the vacuum system. I had a lot of problems with tiny leaks at the connections (flanges) of different beamline components. Finally, I had to apply a Helium leak tester. This device is connected to the prevacuum of the tested system and looks for Helium particles in the extracted gas. Then, Helium is sprayed to the outside of suspicious places of the beamline. If the Helium gas particles get into the chamber through a leak and consequently are pumped into the prevacuum stage, the Helium leak tester notices this immediately. In this way I could remove a big leak directly at the detector flange. I now have end-pressures of the order of $3 \cdot 10^{-10}$ mbar. Nevertheless during the measurement process I have to turn off both the pressure gauge and the ion getter pump at the Dephcon chamber. This leads to higher pressures ($1 \cdot 10^{-9}$ mbar) during the measurements. This concludes the chapter on the experimental implementation of the EES measurement setup with the newly built ultra-compact electronics. It explains how single electrons can be detected and how the accumulated charge at the electrodes of the planar silicon detector is processed and amplified. Finally, to help future physicists that may work on the same topic, it outlines some problems I encountered with the experiment. The next chapter 4 will present results obtained with the new setup.

Chapter 4

Results

This next chapter sets out to present the experimental results obtained in various measurements with the new electronics explained in section 3.6. To illustrate the measurement process, some basic steps like spectrum calibration and data evaluation are examined in sections 4.1 and 4.2 respectively. Section 4.3 outlines some considerations in estimating the approximate error sizes. Next, section 4.4 illustrates the determination of the operating point. The applicability of the new detection electronics was verified at various data points measured on gold (charge dependence, cf. section 4.5) and new data were gathered for Duran glass. This includes the temperature dependence of the electron yield of Duran for various ion species in section 4.6, the angle dependence of the yield in section 4.7 and the velocity dependence in section 4.8.

4.1 Calibration and DP5 Software

The digital pulse processor DP5 sorts the amplified signal into a histogram with a variable number of channels. Next, the spectrum has to be calibrated and the channels have to be matched to their corresponding number of electrons. We know, that the deposited energy of the electrons in the detector is directly proportional to the applied voltage. For a good and reliable calibration of the recorded spectra we need to examine different acceleration voltages. Three sample spectra at different potentials (15 kV, 20 kV and 25 kV) have been recorded for this. The peak positions of the spectra are noted and plotted in a diagram that can be seen in fig. 4.1. Consequently, the 3 lines are fitted with linear fit functions $f(x) = k_i x + d_i$. The fit functions are printed at the top left of the figure. It can be seen that they cross at a single point. Now, due to the linearity of the spectra the peak for the emission of zero electrons would be at this crossing point. In fig. 4.1, the peaks have been identified correctly and the fit coefficients of the corresponding fit function can be used as calibration factors. This calibration method is very useful because sometimes, the first few peaks are not visible due to noise, field emission or if a part of the beam hits the wall of the experimental chamber. Using this method, we can identify the first visible peak as the peak that indeed corresponds to the emission of one electron.
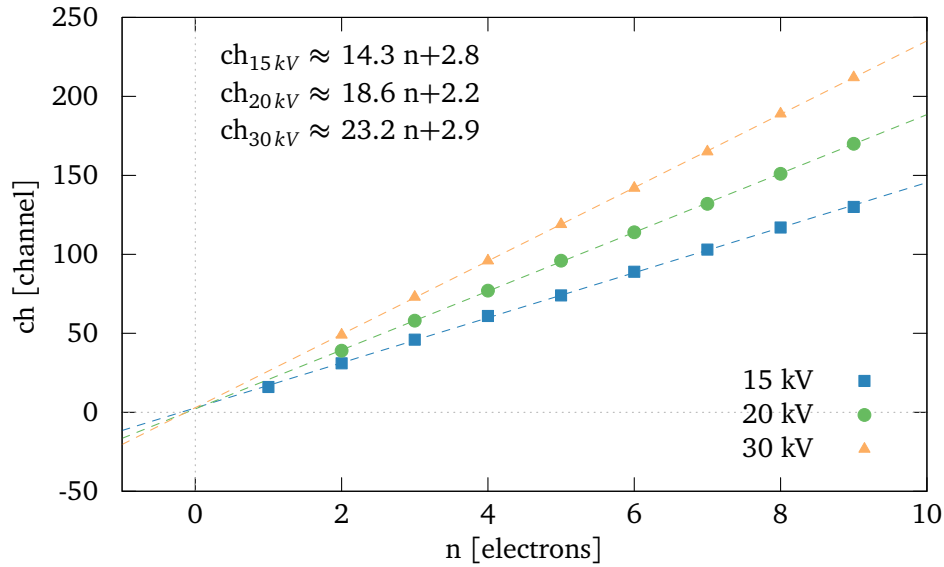
Figure 4.1: In this figure the channels of the peaks corresponding to n simultaneously impinging electrons are plotted. For a good and reliable calibration of the recorded spectra this has to be done for different acceleration voltages that can be seen at the bottom right. The fit functions printed at the top left cross at a single point.

Furthermore, I think it might be very helpful for the reader to get an impression of the MCA software and the settings that were used to measure the spectra. Figure 4.2 shows the main display window of the Amptec DPPMCA (digital pulse processing multi channel analyzer) software. On the left side, a sample spectrum can be seen (Ar^{9+} 4.5 keV ions that impinge on Duran at a temperature of 70 $^\circ C$ and an impact angle of 45° with respect to the surface normal; cf. section 4.6). At low channels the edge of the electronic noise and the first excessive peak corresponding to the emission of a single electron with contributions from field emission can be observed. On the right side, the most important options with their corresponding values are shown. These values have been chosen after a long time of try and test cycles as well as with the help of the integrated digital oscilloscope that can show the shaping of the individual signals. Hence, the peak form of the particular amplified signals can be optimized with the different shaping amplifier settings (flat top width, rise-time, amplifier time constant, etc.). Some important examples of adjustable options are:

- the lower level discriminator (LLD) threshold tells the pulse processor to reject pulses with an amplitude lower than 0.9 % of the maximum value;

- the fast threshold rejects very closely spaced pulses that cannot be distinguished in the slow channel (cf. section 3.6.2);
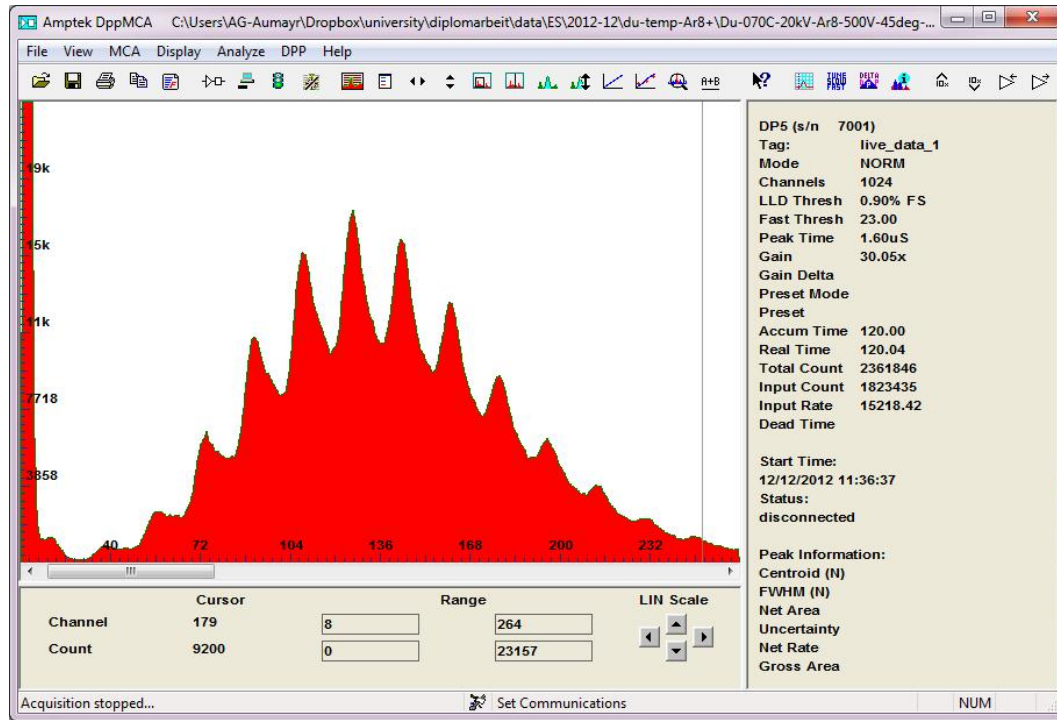
Figure 4.2: Screenshot of the DPPMCA acquisition software with a sample spectrum of 4.5 keV Ar^{9+} impinging on Duran at a temperature of 70 °C and an impact angle of 45° with respect to the surface normal. The toolbar at the top is used to communicate with the DP5 and to adjust the calibration and the acquisition options that can be seen on the right side.

- the total gain is the product of the fine gain and the coarse gain. With a value of 30 the electric signal obtained from the preamplifier is amplified by a factor of 30 before it is sorted into the different channels by the digital MCA.

For a complete description of the different variables please consult the manual of the digital pulse processor DP5 from Amptec available on their website [113].

Another topic is the maximum count rate that can be correctly analyzed. Above a rate of about 15 kHz a non-negligible part (more than 1%) of the incoming pulses start to interfere. With a rise time of 0.2 μs, the DP5 can acquire a periodic signal of 4 MHz which exceeds this rate by far. Thus, the time resolution is mostly limited by the time resolution of the detector itself and by the fact that the pulses are not regularly distributed (pulse pile up). In practice, count rates of up to 40 kHz can be measured. For higher ion currents the effect of pile-up has to be taken into account. Regarding the energy resolution of the whole detection setup, the typical noise of the detector and the preamplifier are of the order of 6.9 keV (cf. section 3.5). The contribution of the DP5 to this error is negligible (Gain Stability < 20 ppm/°C).

4.2 Data Evaluation

In the following paragraphs I want to give the reader a decent summary of the evaluation process. It is not trivial to deduce the electron yield from a given spectrum like the one that can be seen in fig. 4.2. The most important reason is maybe, that the electrons impinging on the PIPS detector have a probability p_b to be backscattered out of the detector before they can deposit all their kinetic energy. Furthermore, it is not known which percentage of the initial energy of the backscattered electrons is deposited in the detector. This fraction ξ that determines the deposited energy of the backscattered electrons plays a crucial role in determining the electron yield. Different methods of analysis have been applied by W. Meissl et al. (cf. [20, p. 74]). The simplest method includes the calculation of the centroid of the spectrum. It is favored over other methods because

- it is independent of the multiplicities; e.g. it is applicable for high and low yield spectra and

- it is very stable and can be automatized in scripts.

This evaluation method will be explained below.

To illustrate the difficulties given above let us assume that n electrons with energy E_n hit the detector simultaneously. Then, $p_b n$ electrons are backscattered. They only deposit a total energy of $p_b n \xi E_n$ instead of $p_b n E_n$. Let E_{det} be the detected energy of a single approaching electron. Therefore,

$$nE_{det} = (n - p_b n)E + p_b n \xi E \tag{4.1}$$

$$nE_{det} = nE(1 - p_b(1 - \xi)) \tag{4.2}$$

$$E_{det}\frac{1}{1 - p_b(1 - \xi)} = E \tag{4.3}$$

$$E_{det}\lambda_\gamma = E. \tag{4.4}$$

The introduced factor is

$$\lambda_\gamma = \frac{1}{1 - p_b(1 - \xi)}. \tag{4.5}$$

It relates the on average deposited or detected energy of a single electron to its actual energy. As we can see, λ_γ is independent of the number n of impinging electrons. This is very crucial because it implies, that not only the detected energy of a single electron scales with λ_γ but also the whole spectrum scales with λ_γ. Hence, we can write:

$$\gamma = \lambda_\gamma(p_b, \xi)C, \tag{4.6}$$

where C is the centroid of the measured spectrum; e.g. the weighted mean value. Let s be the measured signal on channel c. Then the centroid is at channel

$$C = \frac{\sum cs}{\sum s}. \tag{4.7}$$

Given the points from above it can be summarized that the electron yield may be easily extracted from the mean value of a measured spectrum if p_b and ξ are known.
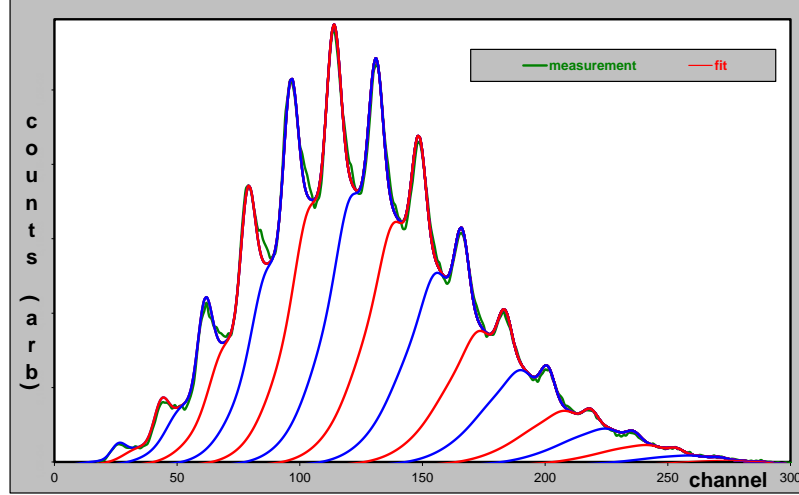

Figure 4.3: Screenshot of a part of the software "Visual-Fit" from M. Simon [20, p. 95] which is included on the DVD supplied with this master's thesis. The x-axis denotes the channel number and the y-axis represents the signal (arbitrary units). Experimental data is shown as a green line. It has been fitted according to the procedure described in [30]. The fit is shown as a sum of contributions for the emission of $1, 2, 3..., n, ...$ electrons. Contributions related to probabilities for the emission of even and odd numbers are colored blue and red, respectively. The area of the nth "stripe" is proportional to the probability W_n in eq. (2.34). The visual fit procedure allows the user to determine the coefficient λ_γ which relates the centroid of a measured EES spectrum to the actual electron yield $\gamma = \lambda_\gamma C$; cf. text. The analyzed spectrum is again from Ar^{9+} 4.5 keV ions impinging on the Duran sample. The Duran has a temperature of 70 °C and the impact angle is 45° with respect to the surface normal. The calculated electron yield γ is 8.6±0.37 electrons which corresponds to a channel of approx. 141. The centroid-yield-factor λ_γ is 1.096.

Simon wrote an application that is called "Visual-Fit" [20, p. 95]. It allows the user to manually (or visually) fit a recorded spectrum. In fig. 4.3 a screenshot of a part of the software is shown. This manual fit procedure is important to determine the coefficients p_b and ξ from above which relate the centroid of a measured EES spectrum to the actual electron yield $\gamma = \lambda_\gamma C$. The analyzed spectrum is again from Ar^{9+} 4.5 keV ions impinging on the Duran sample. The Duran has a temperature of 70 °C and the impact angle is 45° with respect to the surface normal.

Contributions for the emission of a particular number n of emitted electrons (differently colored graphs for even (blue) and odd (red) n in fig. 4.3) to the experimental pulse height spectrum can be derived by a fitting procedure as described in [30]. This procedure includes events with partial backscattering of electrons from the detector. The area of the nth "stripe" is proportional to the probability W_n for the emission of n electrons in a single impact event (cf. section 2.8 and eq. (2.34)). From this test measurement a total electron yield γ of 8.6 ± 0.37 electrons per Ar^{9+} projectile is eval-

uated from the manual fit. This yield is equivalent to a channel of approx. 141. The determined centroid-yield-factor λ_γ is 1.096 corresponding to $p_b = 0.16$ and $\xi = 0.45$

I wrote a Python program *calc-yield.py* which extracts the mean value of a saved spectrum (MCA-file) from the DPPMCA acquisition software that is explained in section 4.1. Moreover, I wrote a script that automatically analyzes all selected MCA-files and calculates the according electron yields γ. These scripts can be found in the folder ~/data/ES/auswertung/neu (cf. section 1.3).

4.3 Estimation of the Measurement Errors

The process of extracting the electron yield γ as a single quantity from an electron spectrum as well as the measurement of the spectrum itself are prone to systematic and statistical errors. In this section I try to outline some considerations in estimating the approximate error size. Again, Simon gives a rather extensive explanation of the different sources for measurement errors [20, p. 99]. The same arguments apply for the data presented in this thesis.

It is important to note, that two types of errors exist: errors regarding the experiment itself and errors due to the evaluation process. The most important experimental error is the uncertainty of the **electron detection efficiency** ϵ. Concerning the evaluation process, the largest errors are the **calibration of the recorded spectra** (cf. section 4.1), the **calculation of the centroid** and the **determination of the centroid-yield-factor** λ_γ described in section 4.2.

The calculation of the centroid is problematic if the multiplicity of the recorded spectrum is small; e.g. the ions have a low electron yield. Then the spectrum may overlap with a possible one-electron-peak from field emission or from ions hitting the wall of the experimental chamber (cf. fig. 4.2). During the measurements presented in this thesis, field emission was not observed. However, for grazing incidence, the incoming beam may be too large. Hence, it does not only illuminate the sample but also passes it and collides with the wall of the experimental chamber. This leads a significant one-electron-peak that can raise difficulties during spectrum evaluation.

It has to be added that the energy resolution of the setup is of the order of 6.9 keV (cf. section 3.5) and that the contribution of the new detection electronics to this error is negligible (Gain Stability $<$ 20 ppm/°C; cf. section 4.1). All in all, a good approximation of the relative measurement error seems to be 2% (cf. [20, p. 99]). The absolute error was determined to be of the order of 0.2 electrons.

On the other hand, it was very hard to get good measurement conditions for lowly charged ions as well as for high acceleration voltages. When the ion source used for these experiments (cf. section 3.1) is operated under these settings, the current of the extracted ions is too high for the PIPS detector. Consequently, the beam has to be dimmed which leads to less than perfect conditions (e.g. measurements at the edge of the beam etc.). Then the systematic error of γ may be somewhat larger. If this is the case it will be indicated in the text.
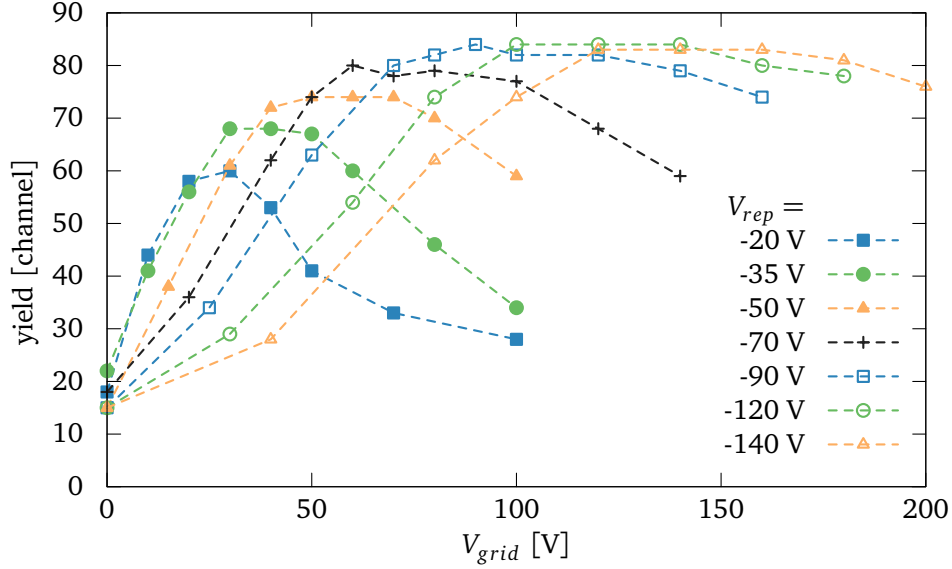
4.4 Determination of the Operating Point

Figure 4.4: This plot shows electron yields (measured in channels; Ar^{9+} 9 keV ions on Au(111) at 45° impact angle) for different grid and electron repeller voltages (V_{grid} and V_{rep}) to determine the operating point. Every single graph resembles a different fixed bias voltage of the electron repeller V_{rep} at varying positive grid voltages V_{grid}.

The previous sections 4.2 and 4.3 explained how the accumulated data was evaluated and how the error of the analyzed data was estimated. Equally important is the optimization of the electron detection efficiency ϵ. In particular, the potentials of four different electrodes can be adjusted to guide as many electrons emitted from the target as possible to the detector. These electrodes are the sample carrier itself, the end-aperture, the electron repeller and the highly transparent grid (cf. section 3.3). Only biasing the two last electrodes improves the electron detection efficiency ϵ.

In more detail, the electrons have to be driven away from the electron repeller and guided towards the highly transparent grid. For this reason, the grid has to be biased positively and the electron repeller negatively. Another advantage of the electron repeller is, that electrons created by ions impinging on the end-aperture are pushed back into the beamline. This greatly reduces the measured one-electron events that do not correspond to electrons emitted from the target (cf. [20, p. 62]).

With this in mind, we want to find a voltage combination that has a very high electron detection efficiency and that will be used as operating point for all subsequent measurements. This is done by measuring the electron yield of a suitable target in dependence on both adjustable voltages the grid voltage V_{grid} and the electron repeller voltage V_{rep}. However, we assume here, that a suitable operating point does not change for different target materials or sample carrier positions. This assumption might not be true, if the energy distribution of the emitted electrons differs for different samples and
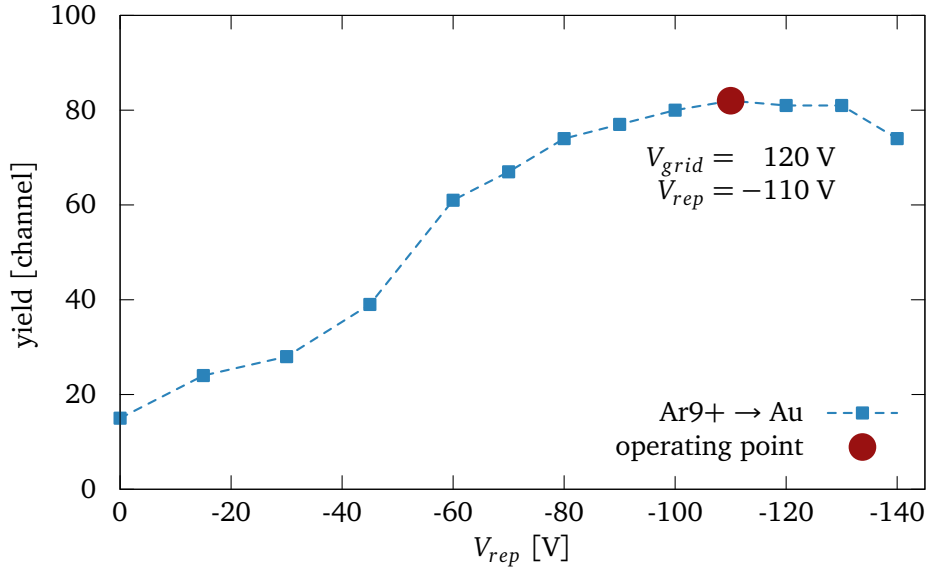
Figure 4.5: More precise measurement of the electron yield (measured in channels; Ar^{9+} 9 keV ions on Au(111) at 45° impact angle) for a fixed grid voltage $V_{grid} = 120$ V at varying electron repeller voltages. The fixed operating point where the highest yield was observed ($V_{rep} = -110$ V and $V_{grid} = 120$ V) is marked in red. Note that the x-axis is reversed and that V_{rep} gets more negative.

ion types and if the sample carrier position severely changes the electrostatic potential inside the experiment chamber.

In fig. 4.4 the electron yields measured in channels for different grid and electron repeller voltages are plotted. Ar^{9+} ions with an energy of 9 keV were colliding with the Au single crystal target (cf. section 3.4.1) at an impact angle of 45°. Every single graph in fig. 4.4 resembles a different fixed bias voltage of the electron repeller at varying positive grid voltages. Going to higher grid voltages the yield curve exhibits a saturation behavior, e.g. with increasing V_{grid} the height of the yield increases up to a certain maximum only to decline if the applied voltage gets too high.

It also can be seen, that the maximum moves to higher V_{grid} and that it gets higher and broader for a more negative V_{rep}. However, the slope of the curve decreases slowly with increasing V_{rep}. Provided that the centroid of the energy distribution of the emitted electrons is located at energies below 50 eV, 120 V seems to be a suitable value for V_{grid}.

To determine the best voltage for the electron repeller, another series of data that is plotted in fig. 4.5 was recorded. It shows a more precise measurement of the electron yield also measured in channels for the fixed grid voltage $V_{grid} = 120$ V at varying negative electron repeller voltages. The fixed operating point where the highest yield at moderate voltages was observed ($V_{rep} = -110$ V and $V_{grid} = 120$ V) is marked in red. This configuration of the guiding potentials ensures a high electron capture efficiency ϵ and the fixation of an operating point facilitates the comparison of different

measurements. The next sections 4.5 to 4.8 present results that have been obtained using this operating point.
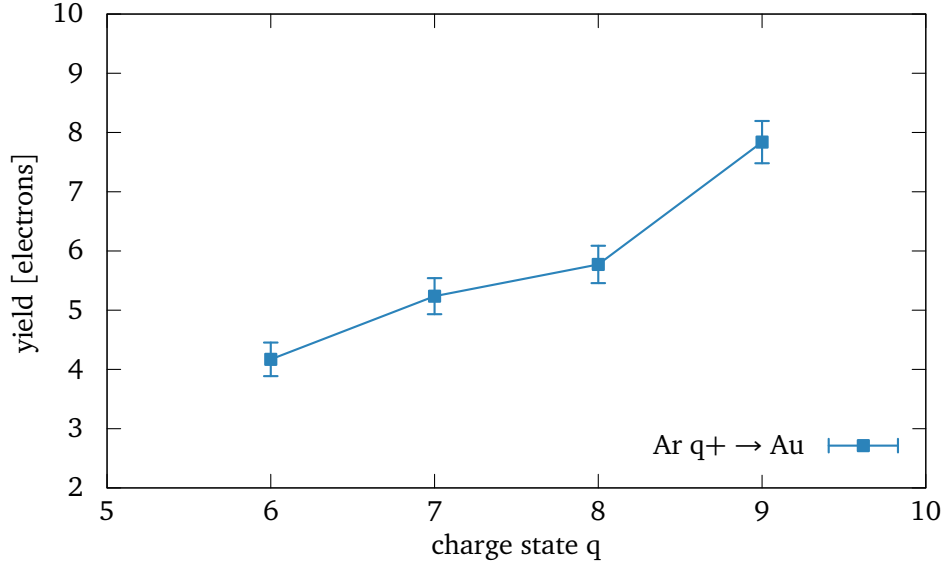
4.5 Demonstration of the new EES setup

Figure 4.6: This plot shows the electron yield of Au bombarded with Ar^{q+} ions with different charge states and energies at an impact angle of 45° with respect to the surface normal. The energy of the impinging ions is q keV.

First measurements were conducted on a circular Au(111) single crystal target with a diameter of approx. 6 mm (cf. section 3.4.1) in order to demonstrate the performance of the new EES detection setup. Gold was chosen as first sample because it is well examined regarding electron emission. Ar^{q+} ($q = 6, 7, 8, 9$) ions with an energy of q keV were shot at this sample at an incident angle of 45° with respect to the surface normal. The appropriate extracted electron yields γ can be seen in fig. 4.6. Note, that not only the charge state, but also the energy of the ions changes due to a fixed acceleration voltage. Nevertheless a larger change of γ can be observed from charge states q= 6 to q= 7 and from q= 8 to q= 9. This is due to the electronic shell structure of Argon ($1s^2 2s^2 2p^6 3s^2 3p^6$).

These yields are compared to previous results by Kurz et al. [31] for normal impact of Ar^{9+} on polycrystalline Au. The following table shows the new data measured with the lightweight electron detection setup as well as extrapolations of the data of Kurz et al. [31].

q	γ [electrons]	γ [electrons], from [31]
6	4.2 ± 0.28	4.0
7	5.2 ± 0.30	5.0
8	5.8 ± 0.31	5.8
9	7.8 ± 0.35	7.8

It can be observed that the electron yields coincide very well within the given measurement errors. However, the following facts have to be considered:

- The data from Kurz et al. was measured at normal impact but these measurements were done at 45° impact angle. Electron emission by low energy highly charged ions is dominated by PE. PE from a Au (single crystal) surface has been shown to depend on the projectile velocity component normal to the surface $v_\perp = \frac{v}{\cos\theta}$ only (cf. section 2.5). Therefore, I had to compare with data from [31] corresponding to the same normal impact velocity. From previous investigations for PE from a Au surface [27] the following empirical relation for PE has been derived $\gamma_P(v,\theta) = c_P^v \frac{1}{\sqrt{v\cos\theta}} + \gamma_P^\infty$ (cf. sections 2.5 and 2.6 and eq. (2.30)). Here, the Ar ions are quite fast so that the contribution of PE in dependence on the impact angle is quite small (if v is large in the formula above the first term remains small for both normal and 45° impact).

- KE becomes increasingly important at these impact velocities. One can calculate the velocities of the Ar^{q+} ions to range from $1.7 \cdot 10^5$ m/s for 6 keV Ar^{6+} to $2.3 \cdot 10^5$ m/s for 9 keV Ar^{9+}. In this velocity regime KE accounts to about $\gamma_K = 1$ e^-/Ar projectile [42]. The measured yield can thus be explained by a dominant contribution from PE plus a minor contribution from KE.

- The data by Kurz et al. [31] has been measured for a polycrystalline Au target, while here, a single crystal Au(111) sample has been used.

In conclusion, the discussion above proves that the new setup is performing properly and that it is apt to reproduce the results obtained from previous experiments.

4.6 Temperature Dependence of the Duran Yield

Irradiation of insulating samples like CaF_2, LiF and Duran (borosilicate glass) might lead to surface charge-up that influences the measured electron yield. In particular, for low temperatures the accumulated charge on the surface cannot be conducted away sufficiently fast. Under these circumstances, a very low electron yield is measured. This effect can be seen in figs. 4.7 and 4.8 where Ar^{q+} ($q = 4, 8$) ions with a kinetic energy of 4 keV hit the Duran sample (cf. section 3.4.1) with an incident angle of 45° with respect to the surface normal. Total electron yields have been measured in dependence on the temperature from room temperature ($T \approx 22$ °C) to approx. 70 °C. For high temperatures, the yields of Ar^{4+} and Ar^{8+} reach 5.8 ± 0.3 and 6.6 ± 0.3 electrons per impinging ion, respectively. Conversely, at room temperature, the yields of Ar^{4+} and Ar^{8+} do not differ greatly and are about 3.8 ± 0.2 electrons per projectile.
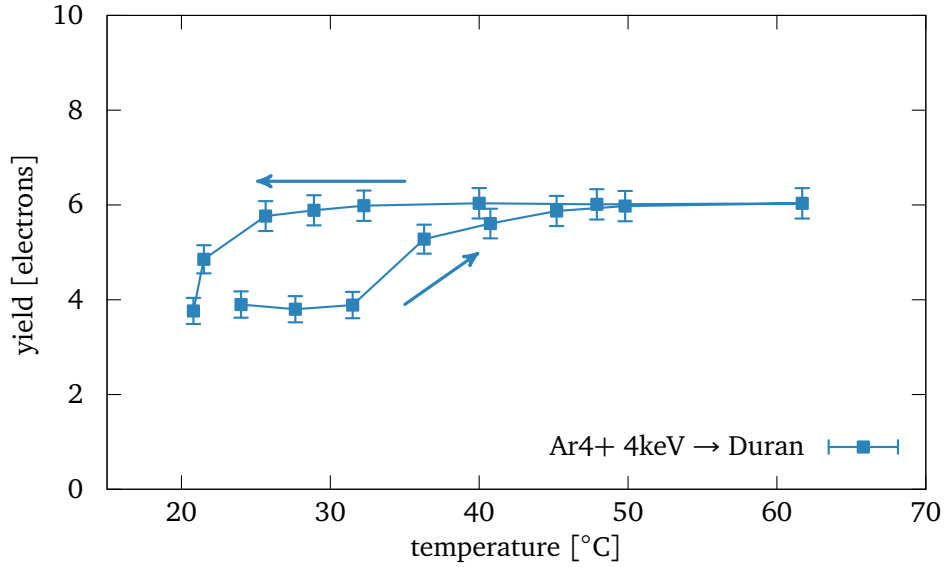
Figure 4.7: In this plot the electron yield of Ar^{4+} 4 keV ions impinging on Duran in dependence on the temperature at 45° impact angle is shown. The ion flux is of the order of 30000 ions/s. The arrows denote the course of time of the measurements.

The arrows in the graphs indicate the time direction of measurement. E.g. for Ar^{4+} (fig. 4.7) the sample was firstly irradiated at room temperature before it was heated up to approx. 70 °C. Lastly it was cooled down again while total electron yields were measured. Measurements that are conducted from low temperatures to high temperatures (e.g. a part of the data found in fig. 4.7) are hard to interpret. This is due to the fact, that the unheated Duran surface can behave in very different ways that are unpredictable and depend on the treatment and condition before the irradiation. For example, the Duran sample might be dirty or it might be charged up due to ions that hit the sample before the actual measurements. This very often was the case because the ion source has to be adjusted before actual measurements can be carried out. This means, that an unknown number of ions of different charge states already hit the sample before spectra are recorded.

However, if the data was measured while heating the target, the electron yield continued to be low until a higher temperature was reached. This might be due to surface impurities or due to a massive accumulation of positive charge at the sample that needs a higher temperature to be conducted away. The transition temperature T_t, that roughly divides the area with high yields and the area with low yields varies greatly for different materials. For Duran the transition temperature T_t has been found to be rather low (approx. 30 °C). Similar data exists from Meissl et al. [16] who measured temperature dependencies for CaF_2 and LiF. The transition temperatures for CaF_2 and LiF were found to be 35 °C and 140 °C, respectively. This temperature is rather high for LiF. That is why Meissl et al. figured out, that the yield levels off at a certain point when
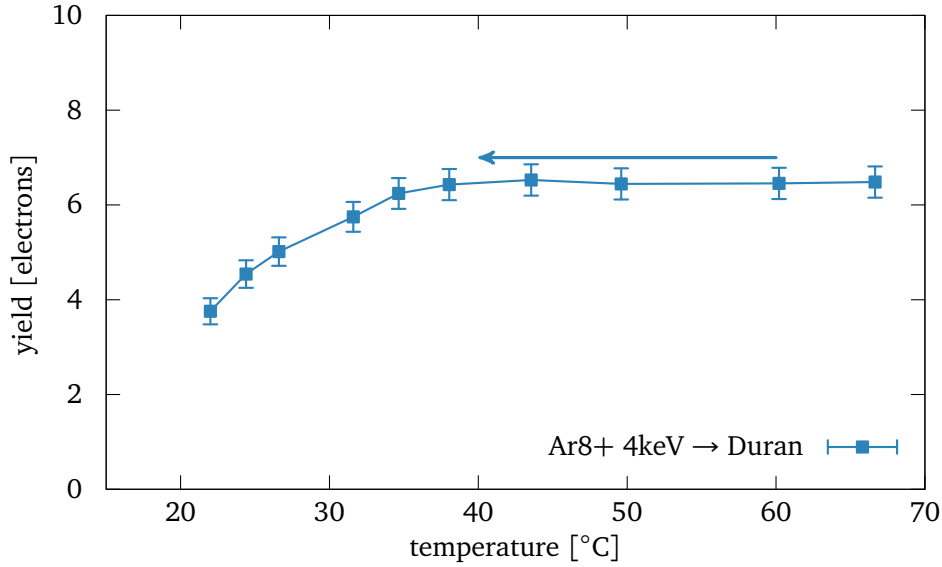
67

Figure 4.8: In this figure the yield of Ar^{8+} 4 keV ions impinging on Duran in dependence on the temperature is plotted. The ions hit the sample at and incident angle of 45° with an ion flux of approximately 40000 ions/s. The arrow denotes the course of time of the measurements.

going to lower temperatures. That is to say, the yield shows a smoothed step function in dependence on the temperature. This point of a constant lower yield could not be reached using Duran and CaF_2 as samples. Considerations stated below suggest that T_t may be dependent on the incident ion flux j_{in} (cf. eq. (4.8)).

We are interested in the reasons of the decline of the total electron yield at low temperatures. As mentioned above, a low conductivity of the sample material leads to a local charge-up and a positive surface charge density. In other words, a positive potential is established at the insulator surface. Under these circumstances, a very low yield is measured because of the following reason: Due to a positive surface potential at the sample, some of the emitted electrons, which have very low energy, are drawn back towards the sample carrier. In the same way, one could only consider the potential differences between the target and the electrodes around it. These electrodes are mainly the wall of the experimental chamber and the electrodes that guide the emitted electrons towards the PIPS detector (electron repeller and highly transparent grid; cf. section 3.3). Provided that the sample surface has a positive potential, the differences of the guiding potentials and the target potential get lower. This leads to a lower detection efficiency ϵ and thereupon to a lower measured total electron yield. Simulations with SimION confirming these considerations have been conducted for different detection geometries and sample carrier potentials by Meissl et al. [21] and in one of my project reports [107].

Given the above, one might consider a very simple model, where the total electron yield only depends on the surface charge density. Basically this surface charge density

q depends on the incident ion flux j_{in} ($\frac{\text{charge}}{\text{unit area} \cdot \text{unit time}}$) and the discharge flux j_d [17] which itself can be characterized by the effective discharge time τ_d. The time derivative of the surface charge density can be written as [17]

$$\dot{q} = j_{in} - j_d(T) = j_{in} - \frac{q}{\tau_d(T)}, \tag{4.8}$$

where T is the temperature. The effective discharge time τ_d basically characterizes how fast the equilibrium state of the surface charge density is reached (half-life). The approximation happens exponentially. The range of τ_d has been estimated for Duran to range from about 4 min for field-driven transport in the bulk to about one month for an unbiased diffusion model (random-walk) [14].
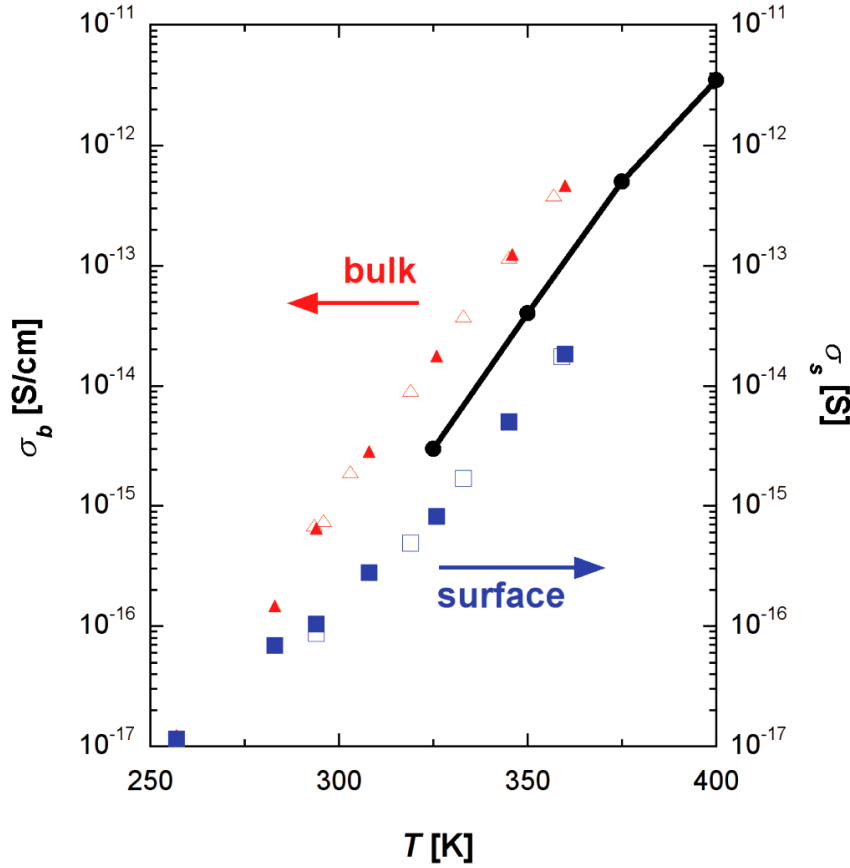
Figure 4.9: This figure taken from [14] shows the electrical surface and bulk conductivity of Duran glass. Triangle (square) symbols denote the results for bulk (surface) conductivity measurements from [14]. The filled symbols represent measurements in vacuum. They are compared to measurements under ambient are (open symbols) conditions. Bulk conductivity values for Pyrex glass (Type 7740, [114]) are shown for comparison (solid line and black dots).

The discharge time τ_d is inversely related to the conductivity of the sample material ($\tau_d^{-1} \propto \sigma(T)$). It has been found that the surface and bulk conductivity of Duran glass show a steep, exponential dependency on the temperature (almost one order of

69

magnitude per $\Delta T = 25\,^\circ$C, see fig. 4.9 and [14]). This means, that the higher the temperature T, the higher the discharge flux j_d and the lower the effective discharge time τ_d. The strong temperature dependence of the conductivity is the key to understand the increase of the electron emission yield at high temperatures.

From eq. (4.8) the equilibrium surface charge density q_{equ} can be calculated to be

$$q_{equ} = \tau_d(T)\, j_{in}. \tag{4.9}$$

Now, let us assume that the total electron yield only depends on the surface charge density. If the measurements are conducted at the equilibrium state (e.g. if we waited long enough so that we could reach this state), the yield should not only depend on the temperature, but also on the incoming ion flux j_{in} that hits the target (cf. eq. (4.9)). It has to be noted, that the time constants of these processes are quite large and that a cold insulating sample may stay charged for hours.
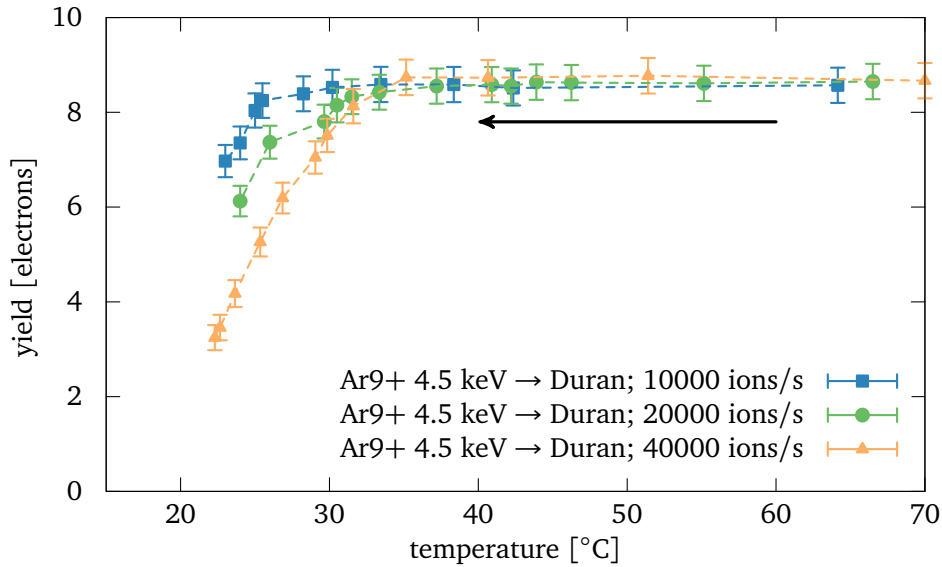
Figure 4.10: This figure shows the electron yield of Ar9+ 4.5 keV ions that impinge on the Duran sample. The yield is plotted vs. the temperature for different ion currents at 45° impact angle. The arrow denotes the course of time of the measurements.

Indeed, good agreement with this reasoning has been found in the experiments. In fig. 4.10 the total electron yields of Ar^{9+} ions with an energy of 4.5 keV impinging on the Duran sample are plotted. Again, the yields were measured starting at high temperatures and going towards lower ones. The impact angle of the ions was 45° with respect to the surface normal. There are three different curves shown. Each curve corresponds to a different ion current (10000, 20000 and 40000 ions/s). Ion fluxes could not be measured directly but the proportions of the ion currents are the same as those of the ion fluxes because the area of the sample remains constant. It can be observed very well that for higher ion fluxes, the total electron yield already starts to

decline at higher temperatures. On the other hand, for lower ion fluxes, we still observe a high yield at temperatures well below 30 °C.

The same observation has been maid by E. Gruber et al. [14]. They increased the incident ion flux j_{in} approaching the capillary and the conductivity $\sigma(T)$ of the capillary material by the same factor. As a result, the guiding angle Φ_c (e.g. the critical angle where the transmitted ion flux has dropped by a factor of $1/e$ [14]) remained constant.

Keeping this in mind, we can further reflect about the functional dependence of the total electron yield $\gamma(q)$ on the surface charge density $q(T, j_{in})$. Applying eq. (4.9) on fig. 4.10, we can tell that the ratio between the surface charge density q is just the ratio between the ion currents. For example, let the subscripts l (for low-count) and h (for high-count) denote the data points that were measured with an ion beam of approx. 10000 and 40000 Ar^{9+} ions/s, respectively. Hence,

$$q_l = \tau_{d,l}(T)\, j_{in,l} \tag{4.10}$$
$$q_h = \tau_{d,h}(T)\, j_{in,h}. \tag{4.11}$$

If the effective surface discharge time only depends on the temperature, one can write:

$$q_l = \tau_d(T)\, j_{in,l} \tag{4.12}$$
$$q_h = \tau_d(T)\, 4j_{in,l}, \tag{4.13}$$

which can be combined to

$$\frac{q_l}{q_h} = \frac{1}{4}. \tag{4.14}$$

This tells us, that the ratios of the surface charge densities are independent of the temperature. Thus, they are constant all along the graphs in fig. 4.10. However, it can be observed that the ratios of the yields $\gamma(q)$ do not behave like this. Consequently, we can conclude, that the functional dependence of γ on $q(T, j_{in})$ is a highly nonlinear one. For instance, in the temperature region that has been considered in these experiments, it could be an exponential dependence (e.g. $\gamma(q) \propto e^{-C\, q_{equ}}$). For the LiF graphs measured by W. Meissl et al. [16] it was found to be a smoothed step function.

It rapidly becomes clear, that the study of the total electron yields in dependence on the temperature and the ion flux is a highly important one. Especially ion guiding through insulating capillaries strongly depends on the surface charge density and therefore on the temperature and on the electron yield [14].

4.7 Angle Dependence of the Duran Yield

This section studies the total electron yield of Duran irradiated by Ar ions of different charge states in dependence on the incident angle of the projectiles. The measurements were performed with a heated Duran sample ($T \approx 70$ °C) so that no effects of the accumulation of surface charges could be observed (cf. section 4.6) and enough electrons
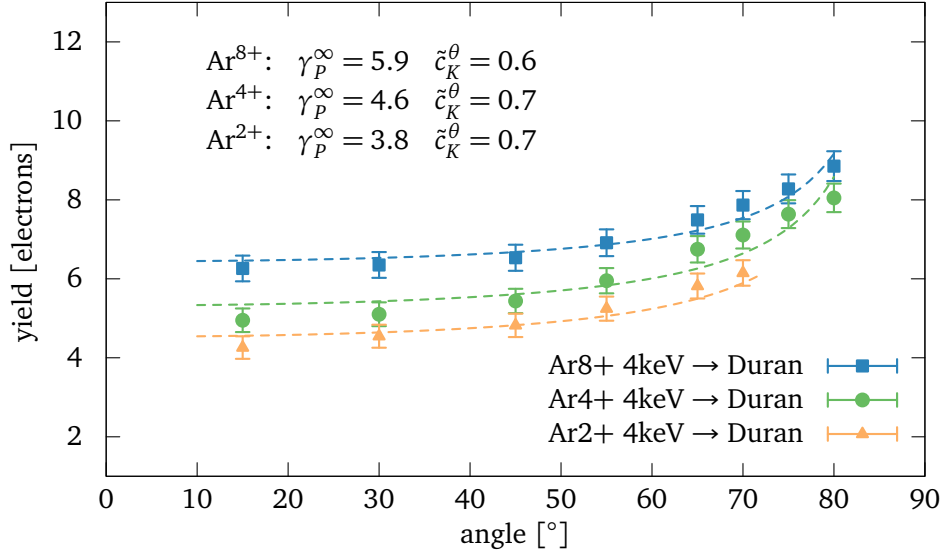
Figure 4.11: In this figure electron yields of Ar ($q = 2, 4, 8$) 4 keV ions that impinge on the Duran sample are shown. The yield is plotted in dependence on the incident angle. The dashed lines represent the different fits according to eq. (4.15) (cf. text). The fit parameters are printed at the top left of the figure.

were provided for high electron emission. Sections 2.4 and 2.5 give an overview of the contributions of the kinetic and the intrinsic potential energy of the approaching ions. Previous measurements from Meissl et al. [16] suggest an empirical fit function according to eq. (2.30). The fit parameters vary greatly for conductors and insulators. It has been found for insulators that the potential emission does not strongly depend on the impact angle and that the kinetic emission varies with the incident ion's impact angle according to an inverse cosine law [98].

Figure 4.11 shows the total electron yields of Ar^{q+} ($q = 2, 4, 8$) ions at a constant kinetic energy of 4 keV impinging on the Duran sample at different impact angles with respect to the surface normal. The detection efficiency ϵ for our setup was found to deteriorate with decreasing impact angle (cf. [20, p. 100]). Therefore, the yields for low impact angles were corrected according to the correction factors given in [20, p. 100]. Indeed, the data points can be well fitted with an inverse cosine law (γ_P^∞ is a constant offset and θ is the impact angle with respect to the surface normal)

$$\gamma(\theta) = \gamma_P^\infty + \tilde{c}_K^\theta \frac{1}{\cos \theta}. \tag{4.15}$$

The fit parameter $\tilde{c}_K^\theta$ is defined as

$$\tilde{c}_K^\theta = c_K(v - v_{th}), \tag{4.16}$$

where v is the velocity, v_{th} is the threshold velocity of kinetic emission and c_K is the coefficient describing the kinetic emission in eq. (2.30). This eq. (4.15) corresponds to eq. (2.30) if c_P^v is very small (e.g. the angle dependence of the PE is negligible). The
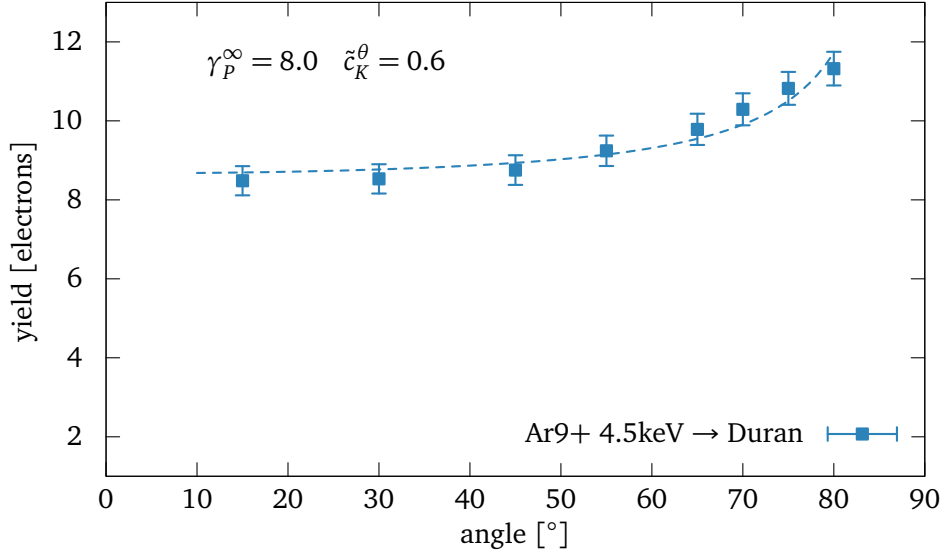
Figure 4.12: In this figure electron yields of Ar9+ 4.5 keV ions that impinge on the Duran sample are shown in dependence on the incident angle. The dashed lines represent the fit according to eq. (4.15) (cf. text). The fit parameters are printed at the top left of the figure.

fitted curves are shown as dashed lines in fig. 4.11. The fitting parameters are shown at the top left corner. It can be observed, that on the one hand $\tilde{c}_K^\theta$ hardly changes in dependence on the charge state of the projectile. On the other hand, the higher the charge state, the higher γ_P^∞. This further underlines that the angular dependence of the total electron yield primarily depends on kinetic emission processes whereas the potential emission remains fairly constant. The same facts were detected by W. Meissl et al. [16] for a LiF sample.

Likewise, in fig. 4.12 measurements for Ar^{9+} ions at different impact angles with respect to the surface normal are shown. The projectiles hit the target with a kinetic energy of 4.5 keV. The dashed line represents the fit according to eq. (4.15). Again, the fit parameters can be seen in the top left. The increase of γ_P^∞ can be confirmed and $\tilde{c}_K^\theta$ nearly remains constant as well. This matches very well the considerations from above.

4.8   Velocity Dependence of the Duran Yield

Finally, total electron yields of Ar ions with different charge states in dependence on the kinetic energy have been measured. Similarly, the sample was heated up to 70 °C to ensure a high electric surface conductivity of the Duran sample.

The results of the determined electron yields are shown in fig. 4.13. Ar^{q+} ($q = 4, 7, 8, 9$) ions with different velocities hit the Duran sample at an incident angle of 45° with respect to the surface normal. Note that the velocity is denoted in units of $[10^3$ m/s$]$. For lower impact velocities the yield should level off at a certain point [16].
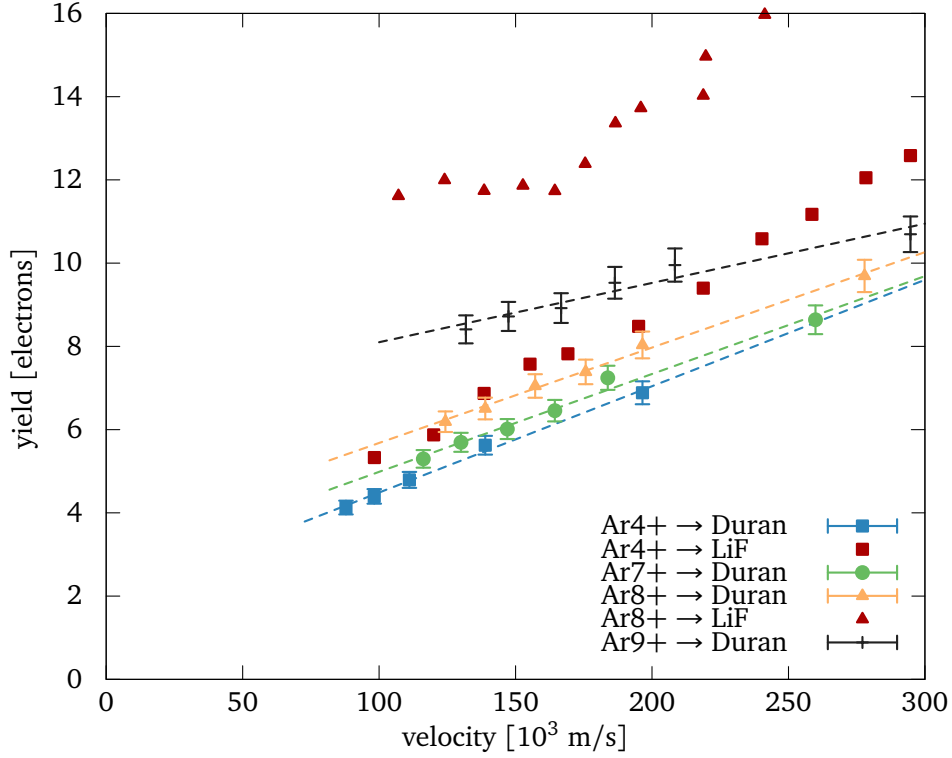
Figure 4.13: This Plot presents Ar yields on Duran in dependence on the velocity for different charge states at 45° impact angle. The dashed lines represent fits of the Duran data according to eq. (4.17) (cf. text). Total electron yields from LiF measured by Kowarik et al. [17] have been added for comparison.

The yields measured for Duran can be compared with measurements of Kowarik et al. on LiF also shown in fig. 4.13. They used a current method (cf. section 2.7) to determine total electron yields from a heated LiF(100) surface. In general, a higher electron yield and a stronger dependence on the kinetic energy of the projectile can be observed for LiF. This results in a larger slope represented by c_K in eq. (2.30). Furthermore, the difference between the electron yield from low energy Ar^{4+} and Ar^{8+} impacts on Duran and LiF is approximately one and six electrons, respectively. This indicates that PE plays a more important role for ion-induced electron emission from LiF than from Duran.

The newly measured data on Duran can be analyzed in the same way as in section 4.7, where the potential emission was supposed to nearly remain constant. Consequently, the empirical fit function of eq. (2.30) can be reduced to

$$\gamma(v) = \gamma_P^\infty + \tilde{c}_K^v(v - v_{th}), \tag{4.17}$$

where γ_P^∞ is a constant offset due to potential emission and $\tilde{c}_K^v$ describes the contributions of kinetic emission. The threshold velocity v_{th} is the boundary where kinetic emission starts (cf. section 2.4). Fit coefficients for v_{th} of the data from Meissl et al. [16] (LiF: $v_{th} \approx 55 \cdot 10^3$ m/s, CaF_2 : $v_{th} \approx 40 \cdot 10^3$ m/s) suggest a v_{th} of approximately $40 \cdot 10^3$

m/s for Duran. This value is used as approximation here, because the exact value for Duran is unknown. The fit parameter $\tilde{c}_K^v$ is defined as

$$\tilde{c}_K^v = \frac{c_K}{\cos\theta} = \frac{2}{\sqrt{2}}c_K.$$

(4.18)

Here, c_K from eq. (2.30) is used and the incident angle was set to $\theta = 45°$. The dashed lines in fig. 4.13 correspond to fits according to eq. (4.17). They represent the experimental data very well. The fit parameters can be found in table 4.1.

ion type	γ_P^∞	$\tilde{c}_K^v$
Ar^{4+}	3.0	$2.5 \cdot 10^{-5}$
Ar^{7+}	3.6	$2.4 \cdot 10^{-5}$
Ar^{8+}	4.3	$2.3 \cdot 10^{-5}$
Ar^{9+}	7.3	$1.4 \cdot 10^{-5}$

Table 4.1: Equation (4.17) was used to fit the data points shown in fig. 4.13. This table shows the parameters γ_P^∞ and $\tilde{c}_K^v$ that minimize the quadratic error.

If we analyze the fit parameters we observe, that the higher the charge state, the higher γ_P^∞ and that $\tilde{c}_K^v$ seems to be nearly independent of the charge state. Only for Ar^{9+} it can be seen that the kinetic contribution is lower. This might be due to a difficult measurement condition because of a very strong Ar^{9+} beam at the highest acceleration voltage (cf. section 4.3).

The fit coefficients from this section 4.8 can be compared with the ones from section 4.7. Regarding the velocity and angle independent potential electron yield γ_P^∞ we find, that it coincides very well. A strong increase of the offset γ_P^∞ can be observed in both measurements with Ar^{9+} ions, where the 2p electron shell has to be broken apart. Furthermore, γ_P^∞ is dependent on the threshold velocity v_{th} for the velocity dependent measurements. Differences might be explained due to the fact, that v_{th} has not been determined exactly for Duran. Similarly, we can compare the contributions of kinetic emission expressed by c_K (cf. eq. (2.30)). The coefficients c_K can be calculated from the parameters $\tilde{c}_K^\theta$ (cf. section 4.7) and $\tilde{c}_K^v$ using eqs. (4.16) and (4.18). The results can be found in table 4.2.

ion type	$\tilde{c}_K^\theta$	c_K from $\tilde{c}_K^\theta$	$\tilde{c}_K^v$	c_K from $\tilde{c}_K^v$
Ar2	0.7	$2.4 \cdot 10^{-5}$	-	-
Ar4	0.7	$1.2 \cdot 10^{-5}$	$2.5 \cdot 10^{-5}$	$1.8 \cdot 10^{-5}$
Ar7	-	-	$2.4 \cdot 10^{-5}$	$1.7 \cdot 10^{-5}$
Ar8	0.6	$0.6 \cdot 10^{-5}$	$2.3 \cdot 10^{-5}$	$1.6 \cdot 10^{-5}$
Ar9	0.6	$0.6 \cdot 10^{-5}$	$1.4 \cdot 10^{-5}$	$1.0 \cdot 10^{-5}$

Table 4.2: Equations (4.16) and (4.18) were used to calculate the corresponding parameters c_K expressing the kinetic emission in eq. (2.30). This table shows the parameters $\tilde{c}_K^\theta$ and $\tilde{c}_K^v$ from sections 4.7 and 4.8 and the appropriate parameters c_K.

The values of c_K calculated from the angle dependent and the velocity dependent measurements do not coincide exactly but they are quite similar. A possible explanation is that the potential emission also shows a small angle dependency. Nevertheless, the whole eq. (2.30) cannot be used as fit function because too many parameters need to be adjusted. Again, the coefficients c_K calculated via eq. (4.16) depend on the threshold velocity v_{th} that was determined using approximations from CaF_2 and LiF. Additionally, it can be seen that the coefficients c_K decline with increasing charge state. From this observation we may conclude that the formula of eq. (2.30) should be altered slightly or that the intrinsic potential energy somehow influences the kinetic emission processes.

This concludes chapter 4 which presents first results of the measurements done with the newly built electronics using digital pulse processing. At the beginning some practical considerations and explained all the steps needed to operate the new setup are outlined. Then, the performance of the new electronics is confirmed by comparing newly measured total electron yields from Au with already existing data from Meissl et al. [16]. Finally, new measurements on Duran are analyzed in the last sections.

Chapter 5

Conclusions and Outlook

During the work on the thesis at hand, an ultra-compact setup for measuring electron emission statistics was designed and built. The performance of this newly constructed setup was tested by measuring ion-induced electron emission from different samples. Additionally, new systematic measurements were conducted on Duran glass (borosilicate glass) to get more insight into the electron emission of this insulator that is used for the production of macrocapillaries that guide highly charged ions [14].

The core of the newly developed measurement electronics constitutes the digital pulse processor unit that contains the DP5 from Amptek. It is a small component that digitally analyzes the signal from the preamplifier and feeds it to the measurement computer. Advantages of the new setup are its improved performance, flexibility (delta mode) and the low cost.

Ion-induced electron emission was measured from a Au single crystal sample to test if the detection setup performs properly. The determined total electron yields from Au agree very well with previous measurements from Kurz et al. [36]. New data was recorded for borosilicate glass (Duran glass). The measured ion-induced electron emission from this glass should lead to a better understanding of the guiding effect [14]. Therefore, electron emission in dependence on the temperature of the sample and the incident angle of the projectiles was examined. For Duran glass the same functional angle dependence was found as for LiF. Furthermore, a strong dependence of the electron yield on the temperature has been measured. A model, where the total yield γ only depends on the surface charge density q was introduced [17] and adapted to the experimental data. Lastly, the dependence of the ion-induced electron emission from Duran on the velocity was compared with previous measurements from LiF [17] and a qualitative agreement has been observed. New computer scripts were written to assure a comfortable and automatic evaluation of the accumulated spectra.

From the above discussion we may further conclude, that theoretical models succeed in describing the underlying physical processes of electron emission [67] but that they, up to now, fail to exactly predict ion-induced electron yields. At the same time, empirical fit functions [16], which include contributions of kinetic and potential electron emission, accomplish to represent the measured yields very well.

It is important to realize, that during the performance of experiments different problems (e.g. with the vacuum or the high voltage) may arise. Usually these issues build an event chain of the form: encounter of the problem, subsequent detection and awareness followed by a solution and progress. For me it was very important to detect this scheme and to realize that problems offer an opportunity for development instead of a period of stagnation and inactivity. In this context I want to give some advice to future master's students:

- trust your experiment but look for defects if the results do not confirm your expectations,
- work calmly and in an accurate way and
- test everything several times before closing and evacuating the beamline.

Given the observations presented in this work I suggest studying ion-induced electron emission from cooled Duran glass so that a saturation of the electron yield at lower temperatures can be measured. Considering the improvement of the experimental implementation of the PIPS detector I propose a superior high voltage protection inside the vacuum chamber to minimize the electron background from electrical discharges. This includes a high quality grid with no possibility of protruding wires and higher distances to the electropolished grounded electrodes and the wall of the experimental chamber.

Finally, the supply of the newly constructed measurement electronics presented in this thesis facilitates the installation of an electron emission detection system at other laboratories. Its compact design and its low cost offer mobility, flexibility and improved measurement conditions. It might allow other groups to easily employ the electron emission statistics technique at their beamlines and use it for diagnostic purposes, surface structure analysis and basic ion-surface collision studies.

Bibliography

[1] F. Aumayr, S. Facsko, A. S. El-Said, C. Trautmann, and M. Schleberger, Journal of Physics: Condensed Matter **23**, 393001 (2011).

[2] F. Aumayr and H. Winter, *Slow Heavy-Particle Induced Electron Emission from Solid Surfaces*, volume 225 of *Tracts in Modern Physics*, chapter 3 "Potential Electron Emission from Metal and Insulator Surfaces", Springer, 2007.

[3] F. Aumayr and H. Winter, Phil. Trans. R. Soc. Lond. A **362**, 77 (2004).

[4] K. Dobes, P. Naderer, C. Hopf, T. Schwarz-Selinger, and F. Aumayr, Nuclear Instruments and Methods in Physics Research Section B: Beam Interactions with Materials and Atoms **286**, 20 (2012).

[5] A. S. El-Said et al., Phys. Rev. Lett. **100**, 237601 (2008).

[6] W. Meissl et al., Journal of Physics: Conference Series **194**, 132027 (2009).

[7] A. S. El-Said et al., Phys. Rev. Lett. **109**, 117602 (2012).

[8] R. Ritter et al., Journal of Physics: Conference Series **388**, 132028 (2012).

[9] N. Stolterfoht et al., Phys. Rev. Lett. **88**, 133201 (2002).

[10] K. Schiessl et al., Phys. Rev. A **72**, 062902 (2005).

[11] P. Skog, H. Zhang, and R. Schuch, Phys. Rev. Lett. **101**, 223202 (2008).

[12] G. Kowarik, R. Bereczky, F. Aumayr, and K. Tőkési, Nuclear Instruments and Methods in Physics Research Section B: Beam Interactions with Materials and Atoms **267**, 2277 (2009).

[13] N. Stolterfoht et al., Phys. Rev. A **83**, 062901 (2011).

[14] E. Gruber et al., Phys. Rev. A **86**, 062901 (2012).

[15] R. J. Bereczky et al., Journal of Physics: Conference Series **388**, 132031 (2012).

[16] W. Meissl et al., e-Journal of Surface Science and Nanotechnology **6**, 54 (2008).

[17] G. Kowarik, E. Gruber, K. Iskratsch, and F. Aumayr, Nuclear Instruments and Methods in Physics Research Section B: Beam Interactions with Materials and Atoms **269**, 964 (2011).

[18] E. Bodewits et al., Nuclear Instruments and Methods in Physics Research Section B: Beam Interactions with Materials and Atoms **269**, 1203 (2011).

[19] E. Bodewits, R. Hoekstra, G. Kowarik, K. Dobes, and F. Aumayr, Phys. Rev. A **84**, 042901 (2011).

[20] M. Simon, Elektronen Emission bei Beschuss von Isolator- und Metalloberflächen mit hochgeladenen Ionen, Master's thesis, IAP Insitute of Applied Physics, Vienna University of Technology, Austria, 2006.

[21] W. Meissl, *The Response of Insulator Surfaces to a Slowly Approaching Highly Charged Ion*, PhD thesis, IAP Insitute of Applied Physics, Vienna University of Technology, Austria, 2008.

[22] D. Winklehner, Electron emission from insulators upon impact of slow highly charged ions, Master's thesis, IAP Insitute of Applied Physics, Vienna University of Technology, Austria, 2008.

[23] G. Kowarik, M. Brunmayr, and F. Aumayr, Nuclear Instruments and Methods in Physics Research Section B: Beam Interactions with Materials and Atoms **267**, 2634 (2009).

[24] G. Kowarik, *The Interaction of Highly Charged Ions with Insulating Matter: Capillary Guiding and Related Phenomena*, PhD thesis, IAP Insitute of Applied Physics, Vienna University of Technology, Austria, 2011.

[25] M. Vana, F. Aumayr, P. Varga, and H. Winter, Nuclear Instruments and Methods in Physics Research Section B: Beam Interactions with Materials and Atoms **100**, 284 (1995).

[26] M. Vana, F. Aumayr, P. Varga, and H. P. Winter, EPL (Europhysics Letters) **29**, 55 (1995).

[27] W. Meissl et al., Nuclear Instruments and Methods in Physics Research Section B: Beam Interactions with Materials and Atoms **256**, 520 (2007).

[28] K. H. Krebs, Annalen der Physik **465**, 213 (1962).

[29] G. Lakits, F. Aumayr, and H. Winter, Review of Scientific Instruments **60**, 3151 (1989).

[30] F. Aumayr, G. Lakits, and H. Winter, Applied Surface Science **47**, 139 (1991).

[31] H. Kurz, F. Aumayr, C. Lemell, K. Töglhofer, and H. Winter, Phys. Rev. A **48**, 2182 (1993).

[32] H. Eder, M. Vana, F. Aumayr, and H. P. Winter, Review of Scientific Instruments **68**, 165 (1997).

[33] C. Lemell, J. Stockl, H. Winter, and F. Aumayr, Review of Scientific Instruments **70**, 1653 (1999).

[34] A. Arnau et al., Surface Science Reports **27**, 113 (1997).

[35] H. Winter and F. Aumayr, J. Phys. B: At. Mol. Opt. Phys. **32** (1999).

[36] H. Kurz, K. Töglhofer, H. Winter, F. Aumayr, and R. Mann, Phys. Rev. Lett. **69**, 1140 (1992).

[37] H. Kurz, F. Aumayr, C. Lemell, K. Töglhofer, and H. Winter, Phys. Rev. A **48**, 2192 (1993).

[38] F. Aumayr et al., Phys. Rev. Lett. **71**, 1943 (1993).

[39] K. Töglhofer et al., EPL (Europhysics Letters) **22**, 597 (1993).

[40] K. Töglhofer, F. Aumayr, and H. Winter, Surface Science **281**, 143 (1993).

[41] H. Kurz et al., Phys. Rev. A **49**, 4693 (1994).

[42] H. Eder, F. Aumayr, and H. Winter, Nuclear Instruments and Methods in Physics Research Section B: Beam Interactions with Materials and Atoms **154**, 185 (1999).

[43] C. Lemell et al., Phys. Rev. Lett. **81**, 1965 (1998).

[44] C. Lemell et al., Phys. Rev. A **61**, 012902 (1999).

[45] H. Eder et al., Phys. Rev. A **62**, 052901 (2000).

[46] A. Mertens et al., Nuclear Instruments and Methods in Physics Research Section B: Beam Interactions with Materials and Atoms **182**, 23 (2001).

[47] A. Mertens et al., Phys. Rev. B **65**, 132410 (2002).

[48] J. Stöckl et al., Nuclear Instruments and Methods in Physics Research Section B: Beam Interactions with Materials and Atoms **193**, 645 (2002).

[49] S. Lederer et al., Phys. Rev. B **67**, 121405 (2003).

[50] J. Stöckl, T. Suta, F. Ditroi, H. Winter, and F. Aumayr, Phys. Rev. Lett. **93**, 263201 (2004).

[51] S. Lederer, H. Winter, H. Winter, and F. Aumayr, The European Physical Journal D - Atomic, Molecular, Optical and Plasma Physics **41**, 505 (2007).

[52] H. Winter et al., Nuclear Instruments and Methods in Physics Research Section B: Beam Interactions with Materials and Atoms **256**, 455 (2007).

[53] F. Aumayr et al., Review of Scientific Instruments **64**, 3499 (1993).

[54] W. Meissl et al., Review of Scientific Instruments **77**, 093303 (2006).

[55] F. Aumayr et al., International Journal of Mass Spectrometry and Ion Processes **163**, 9 (1997).

[56] R. Pfandzelter, T. Bernhard, and H. Winter, Phys. Rev. Lett. **90**, 036102 (2003).

[57] T. Bernhard, M. Baron, M. Gruyters, and H. Winter, Phys. Rev. Lett. **95**, 087601 (2005).

[58] H. Winter, K. Maass, S. Lederer, H. Winter, and F. Aumayr, Phys. Rev. B **69**, 054110 (2004).

[59] L. M. van Kessenich, Nitrogen ion implantation into a diamond crystal, Technical report, IAP Insitute of Applied Physics, Vienna University of Technology, Austria, 2012.

[60] V. P. Ovsyannikov and G. Zschornack, **70**, 2646 (1999).

[61] F. Grossmann et al., Nuclear Instruments and Methods in Physics Research Section B: Beam Interactions with Materials and Atoms **256**, 565 (2007).

[62] M. A. Levine, R. E. Marrs, J. R. Henderson, D. A. Knapp, and M. B. Schneider, Physica Scripta **1988**, 157 (1988).

[63] A. J. G. Martínez, *Quantum interference in the dielectronic recombination of heavy highly charged ions*, PhD thesis, Ruperto-Carola University of Heidelber, Germany, 2005.

[64] E. Galutschek, *Development of a 14.5 GHz all-permanent magnet multicharged ECR ion source for remote operation*, PhD thesis, IAP Insitute of Applied Physics, Vienna University of Technology, Austria, 2005.

[65] E. Galutschek, R. Trassl, E. Salzborn, F. Aumayr, and H. Winter, Journal of Physics: Conference Series **58**, 395 (2007).

[66] H. Gnaser, Interaction of low-energy ions with solids, in *Low-Energy Ion Irradiation of Solid Surfaces*, volume 146 of *Springer Tracts in Modern Physics*, pages 7–82, Springer Berlin/Heidelberg, 1999.

[67] J. Burgdörfer and C. Lemell, *Slow Heavy-Particle Induced Electron Emission from Solid Surfaces*, volume 225 of *Tracts in Modern Physics*, chapter 1 "Theoretical Concepts and Methods for Electron Emission from Solid Surfaces", Springer, 2007.

[68] S. Ossicini, C. Bertoni, and P. Gies, Surface Science **178**, 244 (1986).

[69] R. Ritchie and A. Marusak, Surface Science **4**, 234 (1966).

[70] M. Gottlieb, J. Opt. Soc. Am. **50**, 343 (1960).

[71] T. Okamoto, *Near-Field Optics and Surface Plasmon Polaritons*, chapter Near-Field Spectral Analysis of Metallic Beads, pages 97 – 123, Springer Berlin Heidelberg, 2001.

[72] P. B. Johnson and R. W. Christy, Phys. Rev. B **6**, 4370 (1972).

[73] M. A. Ordal et al., Appl. Opt. **22**, 1099 (1983).

[74] N. W. Ashcroft and N. D. Mermin, *Solid State Physics*, Saunders, 1976.

[75] P. Apell, Nuclear Instruments and Methods in Physics Research Section B: Beam Interactions with Materials and Atoms **23**, 242 (1987).

[76] I. Torrens, *Interatomic Potentials*, Academic Press, 1972.

[77] M. Gryziński, Phys. Rev. **115**, 374 (1959).

[78] L. Vriens, Phys. Rev. **160**, 100 (1967).

[79] R. A. Baragiola, E. V. Alonso, and A. O. Florio, Phys. Rev. B **19**, 121 (1979).

[80] P. A. Anderson, Phys. Rev. **115**, 553 (1959).

[81] R. M. Eastment and C. H. B. Mee, Journal of Physics F: Metal Physics **3**, 1738 (1973).

[82] W. Pong and C. Inouye, Journal of Electron Spectroscopy and Related Phenomena **11**, 165 (1977).

[83] G. Lakits, F. Aumayr, M. Heim, and H. Winter, Phys. Rev. A **42**, 5780 (1990).

[84] H. Winter, S. Lederer, H. Winter, C. Lemell, and J. Burgdörfer, Phys. Rev. B **72**, 161402 (2005).

[85] H. Ryufuku, K. Sasaki, and T. Watanabe, Phys. Rev. A **21**, 745 (1980).

[86] J. Burgdörfer, P. Lerner, and F. W. Meyer, Phys. Rev. A **44**, 5674 (1991).

[87] L. Hägg, C. O. Reinhold, and J. Burgdörfer, Phys. Rev. A **55**, 2097 (1997).

[88] J. Burgdörfer and F. Meyer, Phys. Rev. A **47**, R20 (1993).

[89] A. Bárány and C. J. Setterlind, Nuclear Instruments and Methods in Physics Research Section B: Beam Interactions with Materials and Atoms **98**, 184 (1995), <ce:title>The Physics of Highly Charged Ions</ce:title>.

[90] J. J. Ducrée, F. Casali, and U. Thumm, Phys. Rev. A **57**, 338 (1998).

[91] J. Burgdörfer, *Review Of Fundamental Processes And Applications Of Atoms And Ions*, chapter Atomic Collisions with Surfaces, pages 517–614, World Scientific, 1993.

[92] D. Hasselkamp et al., *Particle Induced Electron Emission II*, volume 123 of *Tracts in Modern Physics*, Springer, 1992.

[93] H. Paul, Nuclear Instruments and Methods in Physics Research Section B: Beam Interactions with Materials and Atoms **247**, 166 (2006).

[94] M. Rösler et al., *Particle Induced Electron Emission I*, volume 122 of *Tracts in Modern Physics*, Springer, 1991.

[95] E. Bodewits, R. Hoekstra, K. Dobes, and F. Aumayr, Phys. Rev. A **86**, 062904 (2012).

[96] L. Wirtz, C. O. Reinhold, C. Lemell, and J. Burgdörfer, Phys. Rev. A **67**, 012903 (2003).

[97] B. Svensson and G. Holmen, Journal of Applied Physics **52**, 6928 (1981).

[98] L. A. Dietz and J. C. Sheffield, **44**, 183 (1973).

[99] H. Winter, *Slow Heavy-Particle Induced Electron Emission from Solid Surfaces*, volume 225 of *Tracts in Modern Physics*, chapter 4 "Kinetic Electron Emission for Grazing Scattering of Atoms and Ions from Surfaces", Springer, 2007.

[100] P. Tiwald, C. Lemell, G. Wachter, and J. Burgdörfer, Journal of Physics: Conference Series **257**, 012012 (2010).

[101] H. D. Hagstrum, Phys. Rev. **96**, 325 (1954).

[102] H. D. Hagstrum, Phys. Rev. **96**, 336 (1954).

[103] H. D. Hagstrum and G. E. Becker, Phys. Rev. B **8**, 107 (1973).

[104] E. Galutschek and H. Winter, *Development of a 14.5 GHz All-Permanent Magnet Multicharged ECR Ion Source for Remote Operation*, PhD thesis, IAP of the Vienna UT, 2005.

[105] K. Halbach, Nuclear Instruments and Methods **169**, 1 (1980).

[106] W. Meissl, Dephcon 1 assembly, Technical report, IAP Insitute of Applied Physics, Vienna University of Technology, Austria, 2004.

[107] D. Schrempf, Ion-induced total electron yields of ultra slow Xe ions impinging on LiF, Technical report, IAP Insitute of Applied Physics, Vienna University of Technology, Austria, 2012.

[108] Duran properties, `http://www.duran-group.com/en/about-duran/duran-properties.html`, Accessed: 25/01/2013.

[109] J. Waclawek, Messung der leitfähigkeit von duran borosilikatglas, Technical report, IAP at the Vienna University of Technology, 2010.

[110] Ortec, *Ortec Catalog - Detectors Section*, 2011.

[111] P. Vacuum, *Vacuum Technology - Know How*, 2009.

[112] E. Gruber, Assembly of the new vacuum system, Technical report, Institute of Applied Physics at the Vienna University of Technology, Vienna, 2011.

[113] Amptek documentation, `http://www.amptek.com/documentation.zip`, Accessed: 26/01/2013.

[114] P. Love, Journal of Physics C: Solid State Physics **16**, 5985 (1983).

List of Figures

List of Tables